



LEIDEN UNIVERSITY

Study of BCG-Subtracted Images of Nearby Clusters

by

Juan Manuel Espejo Salcedo

Advisor:

Dr. Henk Hoekstra

Faculty of Science
Sterrenwacht

July 2017

“Not only is the Universe stranger than we think, it is stranger than we can think..”

Werner Heisenberg

Abstract

Faculty of Science
Sterrenwacht

We study the center of deep imaging data of low redshift massive galaxy clusters where the light from the BGC overwhelms the images from background galaxies and faint cluster members in the cluster core. The proper subtraction of the BCG light is expected to reveal background galaxies that are strongly lensed. We constrain the number of objects that we expect to find in these systems and corroborate these results when subtracting the BCGs and analysing these central regions. Identifying such systems allows for unique follow-up studies such as the true location of the center of the clusters, or the stellar populations in the BCGs that set their formation history. Also, the number density of faint cluster members may tell us something about the dynamical state of the cluster and how BGCs form. The aim of this project is to model the BCG light and search for strong lensing candidates and study the properties of faint cluster members in the core.

Acknowledgements

I would like to thank my supervisor Henk Hoekstra for his support and lessons during these months of research, for his kind supervision and his will to answer my questions. To my parents, who made my journey to the Netherlands possible and to my friends and teammates for a great time during the research ...

Contents

Abstract	ii
Acknowledgements	iii
List of Figures	v
1 Introduction	1
2 Introduction to Gravitational Lensing	7
2.1 Gravitational Lensing formalism	9
3 Determination of the relevant scales	17
3.1 Experiment one: COSMOS field	18
3.2 Experiment two: DM to stellar ratio	19
3.3 Experiment three: Einstein Radius	24
4 Data and analysis	28
4.1 Color images	33
4.2 Star-galaxy determination	36
4.3 Photometric Redshifts	38
5 Conclusions	44

List of Figures

1.1	Enclosed mass for different IMFs in a galaxy	4
1.2	Projected mass of cluster Abell 1201	5
2.1	Types of lensing	8
2.2	Angles in gravitational lensing	9
2.3	Strong Lensing representation	15
2.4	Galaxy Cluster MACS 1206	16
3.1	Galaxies per arcmin	18
3.2	Depth of the different contributions to the COSMOS catalogue	19
3.3	Surface mass density profiles	21
3.4	Enclosed mass and DM to stellar mass ratio for a galaxy cluster	22
3.5	DM and Stellar mass profiles for a massive early type galaxy.	23
3.6	DM and Stellar mass profiles for the “Jackspot” galaxy.	24
3.7	Einstein Ring in LRG 3-757	25
3.8	Reduced shear radial	26
3.9	Magnification radial profile	26
4.1	Segmentation images	30
4.2	Galfit results for Abell 754	31
4.3	All filters’ results for Abell 754	32
4.4	Galfit results for Abell 1413	32
4.5	Color image of A754	33
4.6	Color image of A754 after fitting the bright objects	34
4.7	Einstein ring in color image of A1413	35
4.8	Color images for various clusters	36
4.9	Color Magnitude diagram of Abell 754	37
4.10	Magnitude vs Flux radius of Abell 754	37
4.11	Horizontal cuts to show overestimated background on Abell 1068	39
4.12	Apertures for the aperture photometry procedures on Abell 754	40
4.13	Photometric redshift results for Abell 754	41
4.14	Magnitude distribution of galaxies in Abell 2064	42
4.15	Lensing candidates Abell 2064	43
1	Evolution of the concentration mass relation	46
2	The systematic variation of the IMF in early-type galaxies.	47

Dedicated to my parents, whose love and support are my biggest motivation. . .

Chapter 1

Introduction

Understanding the formation history of stars allows us to comprehend many physical properties of their host galaxies thus providing a useful framework on which to build a more elaborate theory of their subsequent evolution. We might have good ideas and some general agreement in the basics of formation of stars in galaxies, but our observational limitations don't allow us to say much about distant objects which we need to make a more elaborate and complete theory. In principle, we can't assume that all populations of stars have the same formation history in every galaxy and for every epoch of the Universe. The molecular clouds (dense concentrations of interstellar gas and dust) that collapse gravitationally to form stars might or might not create the same mixture of stars in every stellar system since this depends strongly on their composition and the environment in which they collapse, so it is important to see under what conditions we could assume a general trend and what implications in our observations this may have.

For galaxies that are far away, it is impossible to make individual star counts with our current technology, for this reason, their mass-to-light-ratio Υ (which depends on their stellar populations) provides a simple constraint on their number of stars per unit mass given by the initial mass function (IMF), which is a very fundamental and important quantity in the study of stellar systems because it constraints the physics of star formation but also because it allows us to infer stellar masses through observed luminosities as discussed by [Smith & Lucey \(2013\)](#). Everything we know from galaxy evolution is implicitly assuming a certain form of the IMF with very little variations since it is the method we use to connect evolutionary sequences, this of course, given the fact that if every galaxy had its own IMF then it would be too difficult to study their evolution because of the lack of any knowledge about their history.

For stars, measurements of the luminosity function can be used to derive the Initial Mass Function (IMF). For galaxies, this is more difficult because mass to light ratio

(M/L) of the stellar population depends upon the star formation history of the galaxy. A satisfactory determination of the IMF in galaxies is a difficult task, since it depends on very reliable and well-understood data and because it seems to be intimately dependent on the galaxies' formation history ([Cappellari et al. 2012](#)). The determination is usually made by observing star counts, getting the present-day luminosity function (assuming proper mass-luminosity relation and theoretical models that take into account the metallicity), getting the present-day mass function (for some evolutionary tracks and metallicities) and assuming some star formation history to get the IMF. All these assumptions, and the fact that we have to extrapolate these results to systems in which we can't get star counts make the determination very complicated. Moreover, another difficulty of the determination of IMF is that the classical assumption of a single IMF covering the whole mass range is being questioned in favour of a multiple-component IMF to account for possible different formation modes.

Despite these difficulties, we have some observational information about IMFs in galaxies. In the case of spiral galaxies for example, the most commonly used IMFs are Chabrier ([Chabrier 2003](#)) and Kroupa ([Kroupa 2001](#)). With Kroupa favouring a higher number of stars in the low mass regime ($M < 0.5 M_{\odot}$) as compared to Chabrier's. These IMFs are well constrained given the facilities of our observations in our own galaxy. Also, several studies such as the one made by [Brewer et al. \(2012\)](#) suggest that bulges have heavier IMFs than disks as in the case of the commonly used Salpeter IMF by [Salpeter \(1955\)](#).

Although these primary assumptions might not be too far from reality, we must note that when we study dense systems like the brightest cluster galaxies (BCG) in galaxy clusters or giant elliptical galaxies in general, constraining the IMF via M/L poses a greater challenge since masses are more difficult to establish for dynamically-hot systems like them. Measuring Υ in these systems is not a truly accurate constraint on the IMF since we may have different stellar formation histories than the ones associated with galaxies that are being formed now. These objects have a very old origin (although their build up and morphological formation is recent) because their stellar populations are old and they correspond to the highest density peak, so it is difficult to relate their stellar populations accurately.

The M/L depends on galaxy type, but due to the lack of multi-wavelength photometry, it is often assumed that all cluster galaxies are composed of the same stellar population. If one assumes an old stellar population (and therefore a high M/L), the mass of the late-type galaxies (and thus the cluster as a whole) is over-estimated ([Van der Burg et al. 2015](#)).

Mass-to-light ratios of early-type galaxies are of particular interest to understand the tilt of the fundamental plane. Virial relations imply that the effective surface brightness I_{eff} , the effective radius r_{eff} and the central velocity dispersion σ_0 in hot stellar systems are not independent of each other. This is revealed by the fundamental plane of early type galaxies.

This general view shows that when dealing with the evolution of galaxies, there are many things that come together in the context of cosmology but also in the context of stellar astrophysics and they need to be consistent with each other. Additional complications need to be considered when dealing with massive ellipticals and BCGs, one of them is that they have a strong dependency on their non-baryonic matter content which affects the mass-to-light-ratio determination. This dark matter contribution accounts for most of the dynamical mass of galaxies and it's the dominant contribution in most of their spacial scales, specially in the outer regions. The problem would be much easier to study if we only had the stellar mass because the light measurements would be enough to constrain the stellar populations, their evolution and their mass distribution.

Being able to calculate the percentage of dark matter allows us to define the IMF more precisely. So we want to see what fraction of the surface density is given by stars and what are the spatial scales in which DM becomes the dominant contribution to the enclosed mass. DM halos seem to have a diluted profile in comparison to the stellar content of galaxies ([Navarro Frenk & White 1996](#)) so, in principle, there is a region near the center of these massive systems in which the stellar mass is the dominant contribution. This implies that accurate measurements of their luminosity could give precise determinations of their mass to light ratio thus giving us some knowledge of their IMFs.

Recent studies have investigated how the IMF varies with galaxy mass, specially in elliptical galaxies. One of the methods used for this study is a rather indirect method, where galaxy stellar masses are determined from stellar population synthesis models that actually do not resolve the IMF, the results suggest that lower mass early-type galaxies (with dispersions $\sigma \approx 200$ km/s) seem to be consistent with a Milky-Way type IMF (e.g. a Kroupa or Chabrier IMF). In high-dispersion elliptical galaxies, however, stellar mass-to-light ratios are about a factor of 2 times higher than expected from a Kroupa IMF. Some studies indicate that the IMF in massive galaxies seems to be more dwarf dominated than in the Milky-Way so that they can be described by a Salpeter IMF ([Thomas 2014](#)). Also, bulges appear to have heavier IMFs than disks. Figure [1.1] shows the dependence of the enclosed mass of an elliptical galaxy on different IMFs (for a constant mass-to-light ratio).

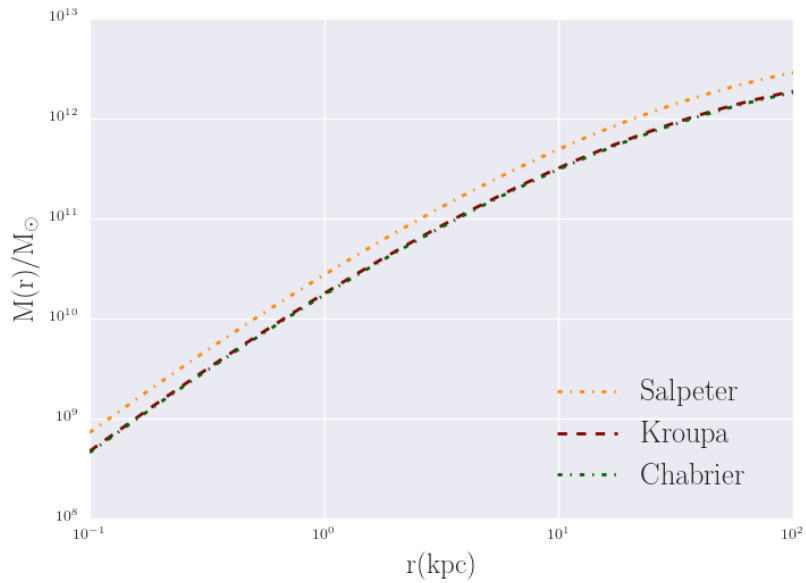


FIGURE 1.1: Enclosed mass for different IMFs in a galaxy of $M_{200} \approx 10^{12} M_\odot$. The figure illustrates the difference of the enclosed mass profile for different assumptions of the IMF in the galaxy. A heavier IMF like Salpeter will yield a higher mass profile with a significant difference from the Chabrier and Kroupa IMFs which have a very subtle difference between them. These profiles are made by integrating the de Vaucouleurs' surface brightness profile and using the mass-to-light ratio for every IMF with the assumption that mass follows light.

As seen in Figure [1.1], the initial mass distribution of galaxies (and consequently their future stellar populations) provides a very powerful constraint on the mass of galaxies so their proper determination is very important. Another example of the variation of the IMF in early-type galaxies can be seen in Figure [2] of the Appendix. Various techniques have been developed to try to understand the stellar populations (consequence of the IMF) that form these massive systems. One of them is by using gravitational lensing of background galaxies (Treu et al. 2010). Modelling the lensing configuration on a massive galaxy like a BCG provides a useful method to determine stellar and dark matter mass contributions in elliptical galaxies, since it is difficult to constrain the IMF via M/L as mentioned before.

Strong lensing measures exactly the total enclosed mass so we need to know how much of the dark matter contribution we need to subtract and on what scales this subtraction is important, the less we have to subtract, the better for the determination of the IMF. If the effect of the IMF is very subtle in the mass vs radius plot, then we would need to know the dark matter distribution very well, but if the effect of the IMF is not very subtle, the less we need to know about the dark matter distribution.

An example of the relevance of the spatial scales is the study of a giant elliptical galaxy (ESO325-G004) by Smith & Lucey (2013), which shows that at very small radii stars

dominate the lensing mass, so that lensing provides a direct probe of the stellar mass-to-light ratio at these scales, with only small corrections needed for dark matter.

Moreover, a more recent study by [Smith et al. \(2017\)](#) characterized the mass profile of the strong lensing BCG of a galaxy cluster (Abell 1201 located at $z = 0.169$) and found that its proper mass modelling needs to include the component of an important central mass which could either be a supermassive black hole or a consequence of a non-uniform stellar mass to light ratio (from a bottom heavy IMF) affecting only the innermost part of the galaxy. His mass modelling is shown in Figure [1.2].

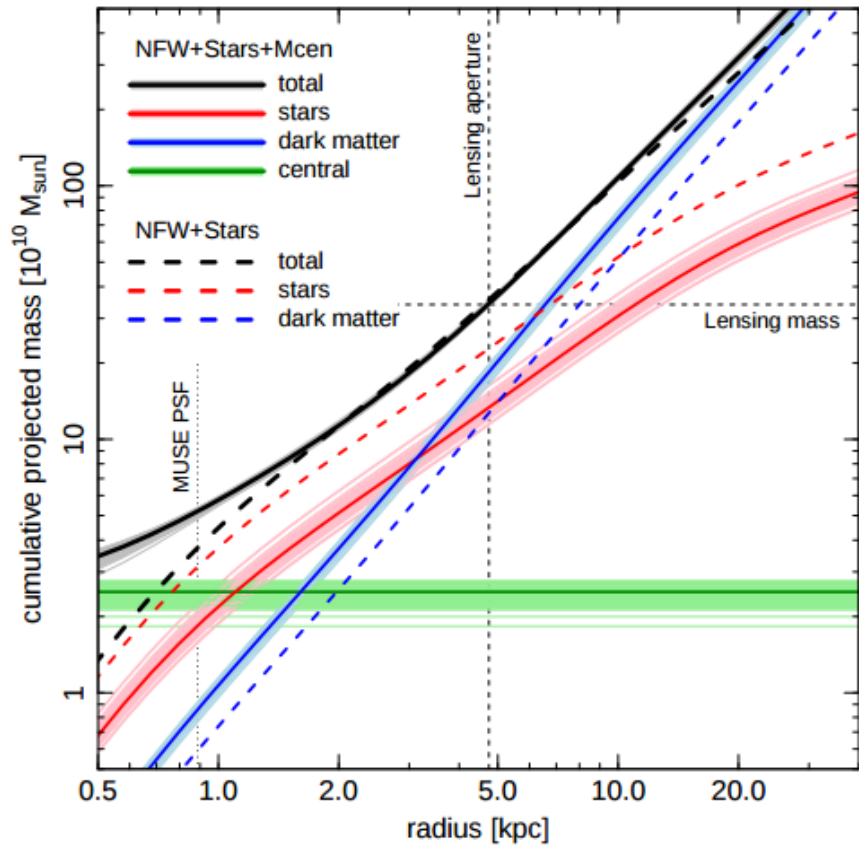


FIGURE 1.2: Cumulative projected mass profile for galaxy cluster Abell 1201 by [Smith et al. \(2017\)](#). The total (solid black) and component (solid colour) indicate the mass profiles including the center mass (NFW+Stars+ M_{cen}). The dashed lines show the best fitting NFW+Stars model without the center mass.

The results of Smith's papers exemplify the importance of the determination of the scales on which strong lensing is useful to characterize the IMF and what scale differences we might encounter when dealing with massive early type galaxies or the characteristic BCGs of galaxy clusters (the latter being one of the main theoretical objectives of this project).

Because lensing gives a very accurate estimate of the total enclosed mass, a lensed system in the core of the galaxy cluster would help us understand the amount of dark matter in that region and could also be interesting for a better determination of DM models.

Finding strong lensing in these systems can also give us information about the location of the mass center of the cluster through the lensing they produce. We usually assume that the centre of galaxy clusters lies in the BCGs ([George et al. 2012](#)) but the real position of the centre in galaxy clusters is still an unsolved problem ([Harvey et al. 2017](#)).

The observational analysis in this project is done for galaxy clusters that might be in the right range to search for gravitational lensing in the inner regions. We use deep data from CFHT and INT in the g, r, i, U bands that allows us to search for interesting targets (lensed systems) and probe the relevant spatial scales. We focus on the brightest cluster galaxy since it is a very massive system that could lens background objects and because photometry measurements can be made very accurately on them in comparison with their neighbouring galaxies.

We subtract the light of the BCGs and search for galaxies that have been strongly lensed (multiple images and arcs) near the radial distance where we expect to find those systems. At the same time, we get several constraints on the amount of objects that we expect to see and over which scales we expect to see them in our data by analyzing the predictions of the theoretical models and by conducting a statistical analysis of extensive data of galaxies at different redshifts. The observational procedures and the search for multiple images using photometric redshifts allow us to corroborate the expected number of lensing candidates.

Chapter 2

Introduction to Gravitational Lensing

As mentioned in Chapter 1, the problem of determining the mass component of a BCG in a galaxy cluster is not trivial whatsoever but we can get some constraints by the use of gravitational lensing in these massive objects. The understanding of the gravitational lensing formalism teaches us how to calculate the total mass content of the lense (which in this case is our target of study) and thus provides a powerful tool to properly model the mass of the BCGs by their strong gravitational lensing effects on background galaxies.

For the aims of this project, what we need is to understand the effects of gravitational lensing on the light of background objects without giving details on a more complicated theory of the nature of these effects i.e solutions of Einstein's field equations around massive objects. The basic principle behind gravitational lensing is that light rays don't always travel in straight lines through spacetime but their trajectories are modified when they travel close to the potential well (the distortion of space time) of massive objects, the effect is the distortion of the shapes of the background objects. In the case when the lensing is caused by very massive objects like galaxies and clusters of galaxies, these effects can be so strong that the background objects can appear to be in different positions (multiple images) and in some cases the distortion of these shapes can be such that the background object appears to be a ring around the massive lensing object (lense). These are analogous effects to the ones caused by optical lenses.

Although the discovery of gravitational lensing was made only in the past century, the possibility that there could be such a deflection had been suspected much earlier, by Newton and Laplace among others ([Narayan et al. 1995](#)). Johann Gerog von Soldner in 1801 calculated the magnitude of the deflection due to the Sun, assuming that light

consists of material particles and using Newtonian gravity. Later, Einstein (in 1911) employed the equivalence principle to calculate the deflection angle and re-derived Soldners formula. Later yet, in 1915 Einstein applied the full field equations of General Relativity and discovered that the deflection angle is actually twice his previous result, the factor of two arising because of the curvature of the metric. According to this formula, a light ray which tangentially grazes the surface of the Sun is deflected by 1.7 arcsec. Einsteins final result was confirmed in 1919 when the apparent angular shift of stars close to the limb of the Sun was measured during a total solar eclipse in 1920. The quantitative agreement between the measured shift and Einsteins prediction was immediately perceived as compelling evidence in support of the theory of General Relativity.

Gravitational lensing can be separated into two main categories which are its two most important ways to manifest.

- 1. Strong lensing:** Where there are easily visible distortions on the shape of background objects such as the formation of Einstein rings (where the alignment between the source, lens and object allows for an optical effect in which the observer sees a full ring surrounding the lens), arcs (the alignment is not good enough for the formation of a ring, but only for segments of it with the shape of arcs), and multiple images of the same object.
- 2. Weak lensing:** Where the distortions of background sources are much smaller and can only be detected by making a statistical analysis of a large number of sources that allows to find coherent alignments on their distortions.

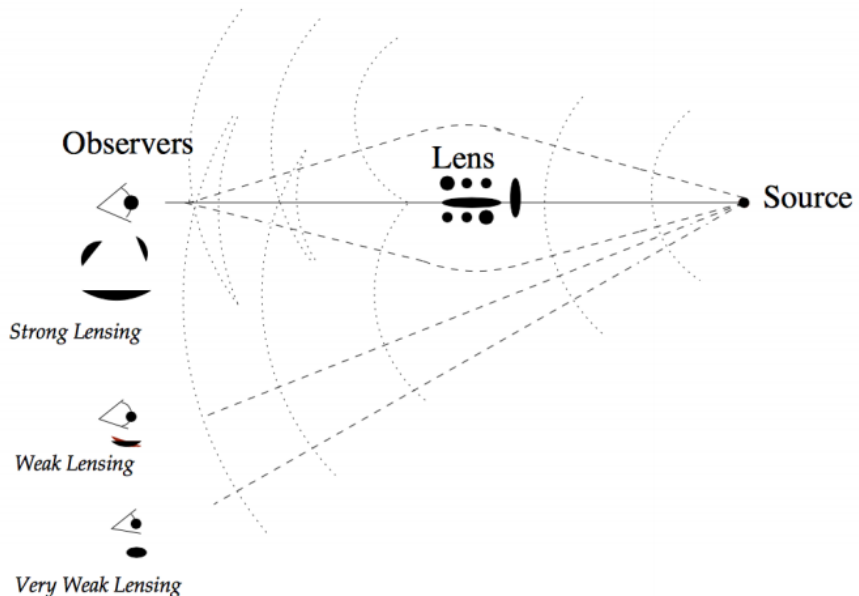


FIGURE 2.1: Sketch of the main characteristics of the types of lensing. Figure by [Courbin et al. \(2002\)](#)

Figure [2.1] sketches the effects of gravitational lensing in the strong, weak and very weak lensing regimes. As seen in the figure, under certain conditions the background source can be seen in multiple images and “arcs” surrounding the lensing object, which is the strong lensing regime and will be the useful regime for this work.

2.1 Gravitational Lensing formalism

For the generalities of gravitational lensing we follow the order given in a review by Meneghetti (2003). The first important quantity is the deflection angle which is the measure of the angular distance that has been deflected and which is linearly dependent on the mass M . This dependence ensures that the angles of deflection of an array of lenses can be superposed linearly.

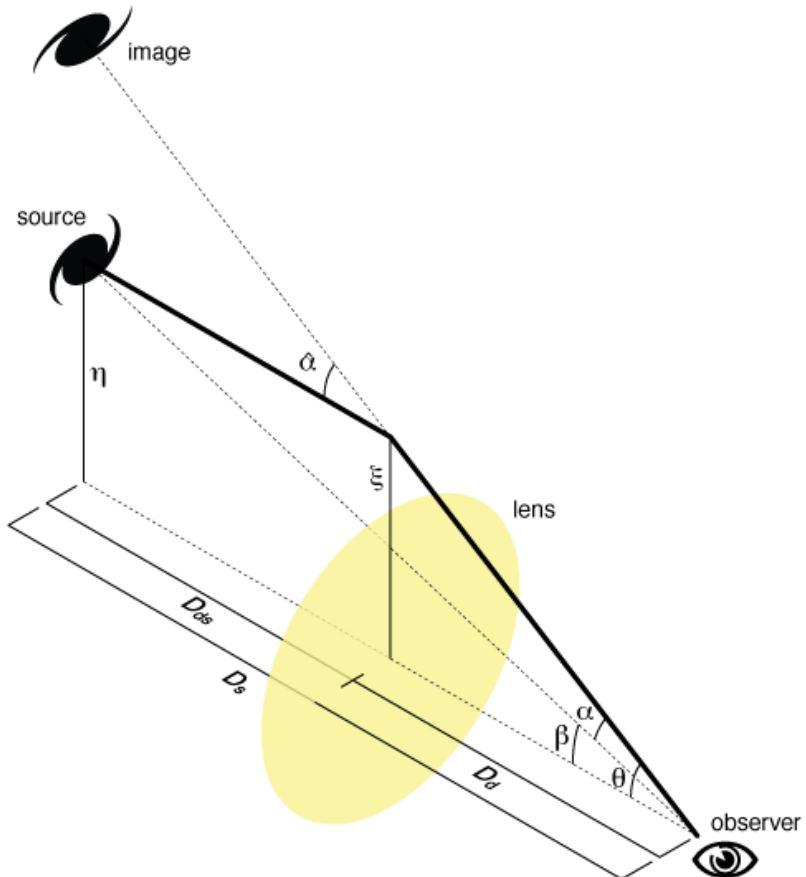


FIGURE 2.2: Sketch of a lensing configuration, where D_{ls} is the distance from the lens to the source, D_s is the distance from the observer to the source and D_o is the distance from the observer to the source. Image by Michael Sachs, Wikipedia.

Figure [2.2] is a sketch of a typical gravitational system. The lensing mass is located at an angular diameter distance D_d and it deflects the light rays coming from a source at an angular distance of D_s .

The optical axis is perpendicular to the lens and source planes and passes through the observer. We measure the angular positions on both planes with respect to this reference direction. The source is at the angular position $\vec{\beta}$ and lies on the source plane at a distance $\vec{\eta} = \vec{\beta}D_s$ from the optical axis. The deflection angle $\hat{\vec{\alpha}}$ of the light ray comes from the source and has impact parameter $\vec{\xi} = \vec{\theta}D_d$ on the lens plane. Due to this deflection, the observer receives the light coming from the source as if it was emitted at the angular position $\vec{\theta}$.

If $\vec{\theta}$, $\vec{\beta}$ and $\hat{\vec{\alpha}}$ are small, the true position of the source and its observed position on the sky are related by a very simple relation, obtained by a geometrical construction. This relation is called the lens equation and is written as

$$\vec{\theta}D_s = \vec{\beta}D_s + \hat{\vec{\alpha}}D_{ds} \quad (2.1)$$

where as seen in Figure [2.2], D_{ds} is the distance between the lens and the source.

Defining the reduced deflection angle

$$\vec{\alpha}(\vec{\theta}) \equiv \frac{D_{ds}}{D_s} \hat{\vec{\alpha}}(\vec{\theta}) \quad (2.2)$$

And from equation 2.1 we get

$$\vec{\beta} = \vec{\theta} - \vec{\alpha}(\vec{\theta}) \quad (2.3)$$

If we had N point masses sparsed on a plane, with positions ξ_i and masses M_i , then the deflection angle (as a function of the impact parameter) would be:

$$\hat{\vec{\alpha}}(\vec{\xi}) = \sum_i \hat{\vec{\alpha}}_i(\vec{\xi} - \vec{\xi}_i) = \frac{4G}{c^2} \sum_i M_i \frac{\vec{\xi} - \vec{\xi}_i}{|\vec{\xi} - \vec{\xi}_i|^2} \quad (2.4)$$

Fortunately, in most three dimensional distributions of matter (even in the case of lensing by massive objects like galaxy clusters) the physical size of the lens is generally much smaller than the distances between the observer, the lens and the source. This means that the deflection of light takes place in a very thin and short section of its path

to the observer. Given this, we can use the *thin screen approximation*: “The lens is approximated by a planar distribution of matter, the lens plane”. Also the sources can be treated as if they lie on a plane which is called the source plane.

Another useful quantity in characterizing a gravitational lensing system is the surface density which fully describes the lensing matter distribution

$$\Sigma(\vec{\xi}) = \int \rho(\vec{\xi}, z) dz \quad (2.5)$$

where $\vec{\xi}$ is a two-dimensional vector on the lens plane and ρ is the three dimensional density.

The most interesting physics of the simple lens equation arises because $\vec{\alpha}$ depends on $\vec{\theta}$. Now, we can characterize an extend the distribution of matter by its effective lensing potential, which is obtained by projecting the three-dimensional Newtonian potential on the lens plane and scaling it accordingly

$$\hat{\Psi}(\vec{\theta}) = \frac{D_{ds}}{D_d D_s} \frac{2}{c^2} \int \Phi(D_d \vec{\theta}, z) dz \quad (2.6)$$

This lensing potential satisfies two important properties:

- 1) The gradient of Ψ gives the scaled deflection angle:

$$\vec{\nabla}_x \Psi(\vec{x}) = \vec{\alpha}(\vec{x}) \quad (2.7)$$

- 2) The Laplacian of Ψ gives twice the convergence

$$\Delta_x \Psi(\vec{x}) = 2\kappa(\vec{x}) \quad (2.8)$$

where the convergence is defined as a dimensionless surface density

$$\kappa(\vec{x}) \equiv \frac{\Sigma(\vec{x})}{\Sigma_{cr}} \quad \text{with} \quad \Sigma_{cr} = \frac{c^2}{4\pi G} \frac{D_s}{D_d D_{ds}} \quad (2.9)$$

Σ_{cr} is called the critical surface density and it characterizes the lens system and which is a function of the angular diameter distances of lens and source. It is also very useful to quantify the distortion of shapes of background objects since it can be studied using statistical approaches on the observations.

It is then useful to introduce the mathematical formalism of the distortion. As mentioned at the beginning of this chapter, one of the main features of gravitational lensing is that it distorts the shapes of the sources, this is particularly evident when the source has no negligible apparent size. In some cases the background galaxies can appear as very long arcs in galaxy clusters as in the case of strong gravitational lensing.

The effect of distortion takes place because light bundles are deflected differentially. In the ideal case, the shape of the background images can be determined by solving the lens equation for all the points within the extended source. In particular, if the source is much smaller than the angular size on which the physical properties of the lens change, the relation between the source and image positions can locally be linearised. Mathematically this means that the distortion of images can be described by the Jacobian matrix

$$A \equiv \frac{\partial \vec{y}}{\partial \vec{x}} = \left(\delta_{ij} - \frac{\partial \alpha_i(\vec{x})}{\partial x_j} \right) = \left(\delta_{ij} - \frac{\partial^2 \Psi(\vec{x})}{\partial x_i \partial x_j} \right) \quad (2.10)$$

where x_i indicates the i -component of \vec{x} on the lens plane. It shows that the elements of the Jacobian matrix can be written as combinations of the second derivatives of the lensing potential. It is useful to use the shorthand notation

$$\frac{\partial^2 \Psi(\vec{x})}{\partial x_i \partial x_j} \equiv \Psi_{ij} \quad (2.11)$$

Now, by splitting off an isotropic part from the Jacobian

$$\left(A - \frac{1}{2} \text{tr} A \cdot I \right)_{ij} = \begin{pmatrix} -\frac{1}{2} (\Psi_{11} - \Psi_{22}) & -\Psi_{12} \\ -\Psi_{12} & \frac{1}{2} (\Psi_{11} - \Psi_{22}) \end{pmatrix} \quad (2.12)$$

we get the shear matrix, which is an antisymmetric, trace-free matrix that quantifies the projection of the gravitational tidal field (the gradient of the gravitational force), which describes distortions of background sources. This allows us to define the pseudo-vector $\vec{\gamma} = (\gamma_1, \gamma_2)$ on the lens plane, whose components are

$$\gamma_1(\vec{x}) = \frac{1}{2} (\Psi_{11} - \Psi_{22}) \quad \text{and} \quad \gamma_2(\vec{x}) = \Psi_{12} = \Psi_{21} \quad (2.13)$$

This is called the shear. The eigenvalues of the shear matrix are

$$\pm \sqrt{\gamma_1^2 + \gamma_2^2} = \pm \gamma \quad (2.14)$$

Thus, there exists a coordinate rotation by an angle ϕ such that

$$\begin{pmatrix} \gamma_1 & \gamma_2 \\ \gamma_2 & -\gamma_1 \end{pmatrix} = \gamma \begin{pmatrix} \cos 2\phi & \sin 2\phi \\ \sin 2\phi & -\cos 2\phi \end{pmatrix} \quad (2.15)$$

And for the trace we have

$$\frac{1}{2} \text{tr} A = (1 - \kappa) \delta_{ij} \quad (2.16)$$

Thus the Jacobian becomes

$$A = \begin{pmatrix} 1 - \kappa - \gamma_1 & -\gamma_2 \\ -\gamma_2 & 1 - \kappa + \gamma_1 \end{pmatrix} \quad (2.17)$$

Where κ is the convergence that determines the magnification and γ_1 and γ_2 are the shear components that determine the distortion of the background objects. More precisely, the convergence describes the isotropic focusing of light rays while the shear describes the effect of tidal gravitational forces. Convergence acting alone leads to an isotropic magnification or demagnification while the shear induces distortions in the shapes of lensed images ([Wright & Brainerd 1999](#)).

Unless we have a measurement of the intrinsic size or magnification of a galaxy we cannot measure the shear γ but only the reduced shear which is given by:

$$g = \frac{\gamma}{1 - \kappa} \quad (2.18)$$

Calculating the reduced shear for different redshifts will give us a constraint about the location of the Einstein ring on each cluster (where the reduced shear diverges). Finally, we can introduce another useful quantity in the characterization of gravitational lensing systems. The *magnification* is quantified by the inverse of the determinant of the Jacobian matrix. For this reason, the matrix $M = A^{-1}$ is called the *magnification tensor*, and we define

$$\mu \equiv \det M = \frac{1}{\det A} = \frac{1}{(1 - \kappa)^2 - \gamma^2} \quad (2.19)$$

The magnification will be an important and useful quantity in our work since its calculation will give us a hint about the radius of the Einstein rings (where the magnification

is infinite). The eigenvalues of the magnification tensor measure the amplification in the tangential and in the radial direction and are given by

$$\mu_t = \frac{1}{\lambda_t} = \frac{1}{1 - \kappa - \gamma} \quad \text{and} \quad \mu_r = \frac{1}{\lambda_r} = \frac{1}{1 - \kappa + \gamma} \quad (2.20)$$

The magnification is ideally infinite where $\lambda_t = 0$ and where $\lambda_r = 0$. These two conditions define two curves in the lens plane, called the tangential and the radial critical line, respectively. An image forming along the tangential critical line is strongly distorted tangentially to this line. On the other hand, an image forming close to the radial critical line is stretched in the direction perpendicular to the line itself.

At last, it is necessary to introduce a simple way to characterize the physical scale in which we expect to find strong lensing. This can be done by calculating the characteristic radius of gravitational lensing which is called the **Einstein radius** (radius of the Einstein rings). Since we don't have information about the mass of the system, we must use an approximation that relates known quantities such as the velocity dispersion σ . In the approximation of the single isothermal sphere (see Appendix), the line of sight velocity dispersion is constant as well as the gradient of the projected potential, therefore the deviation angle is constant and the Einstein radius R_E can be obtained from the velocity dispersion as

$$R_E = 4\pi \left(\frac{\sigma}{c}\right)^2 \frac{D_{ds}}{D_s} \quad (2.21)$$

The calculation of the Einstein radius for the galaxy clusters (assuming different source distances constrained by some assumptions explained in Chapter 3) is relevant because it allows us to define the important regions on which to focus the analysis and the search for lensing candidates.

In the inner region of galaxy clusters we are in the strong lensing regime so we will focus our discussion only on strong lensing (weak lensing is not relevant for this work) i.e we search for multiple images and arcs in the inner regions of the galaxy clusters. Figure [2.3] is a representation of a strong lensing system in which a background galaxy is lensed by a cluster of galaxies and produces multiple images and arcs observed by our telescopes. It represents the ideal case in our study.

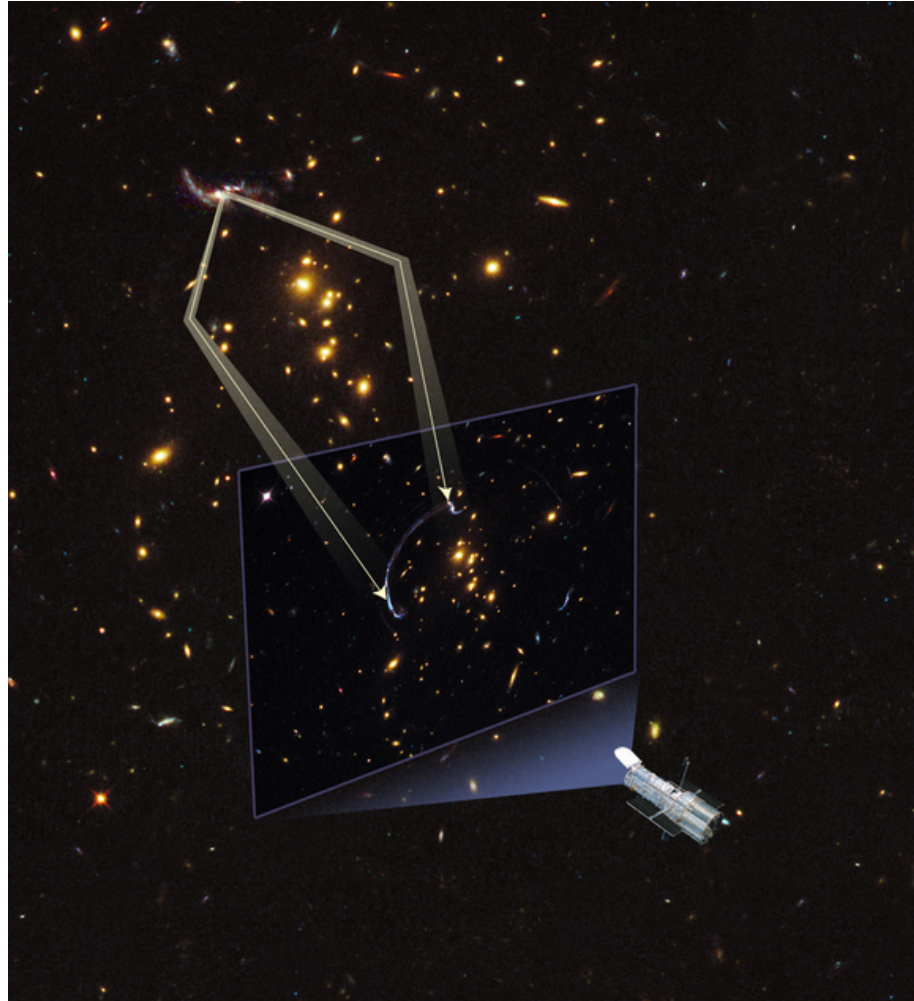


FIGURE 2.3: Representation of strong lensing by a galaxy cluster. It displays arcs and multiple images of a background object, as expected for strong gravitational lensing in these massive systems. Credits to NASA.

A real example of a strongly lensed system (with arcs and multiple images) is shown in Figure [2.4] which shows a composite color image of a galaxy cluster (MACS 1206 which lies at $z = 0.439$) taken by the HST. In this system, astronomers counted 47 multiple images of 12 newly identified galaxies. It shows the importance of the correct subtraction of the light of the BCG which is the overwhelming feature in the cluster luminosity.



FIGURE 2.4: Strong and weak lensing galaxy cluster MACS 1206 ($z = 0.439$), credits to NASA Hubble Space Telescope.

The framework of gravitational lensing provides a scenario on top of which we conduct several experiments and analysis of the data. In the next chapter we focus our attention on understanding on what scales we can use gravitational lensing to study galaxy clusters at low redshifts, and how many lensed objects we expect to find in them.

Chapter 3

Determination of the relevant scales

In this project we base our analysis on the center of galaxy clusters at low redshift so it is necessary to understand which scales will be relevant for our studies. In order to calculate the range of scales that we will probe in the observational procedures on Chapter 4 we will do three separate experiments.

The first experiment is the calculation of the number of objects that we would expect to be lensed near the cluster centres by using a very extensive catalogue of galaxies located at different redshifts. Calculating the amount of galaxies that we should see in the vicinity of the BCG (with their reported redshift) given the characteristics of our data gives us an idea on how many of those objects could in principle be lensed by the BCG and what is the redshift range on which we should focus our attention.

The second experiment consists on doing the mass modelling of the cluster for its stellar and dark matter content to see on which scale stars are the main component of the enclosed mass that lenses background objects (this will suggest where the determination and characterisation of the IMF can be done with a good degree of confidence).

The third one is the calculation of the expected Einstein radius for objects located at different redshifts which will help us define the most relevant regions to look for lensing candidates.

3.1 Experiment one: COSMOS field

For our first experiment we need a very large catalogue of galaxies (with their spatial locations and redshifts) that allows us to get the average number of galaxies contained in certain redshift range. In order to do this, and put it into the context of our work, we select a square region on the data (similar to the effective area surrounding the BCGs of our sample) and see how many galaxies are contained in that region with their corresponding redshifts and with their corresponding magnitude in the r band. This will thus give us the number of galaxies that we would expect to see with the sensitivity of our data and will also help us constrain the redshifts to probe.

For this purpose we make use of the COSMOS2015 catalogue (Laigle et al. 2016) which contains half a million objects in a range of $1 < z < 6$. Ricardo Herbonnet (private communication) matched the CFHT data to this catalogue so we use his matched data in the r band which contains a total of 133,348 galaxies in the 2 degree COSMOS field. We count the amount of galaxies for different magnitudes in redshift bins of $0.2z$ for this filter. These numbers represent the expected number of galaxies in the background of the lens objects of our sample as seen in Figure [3.1].

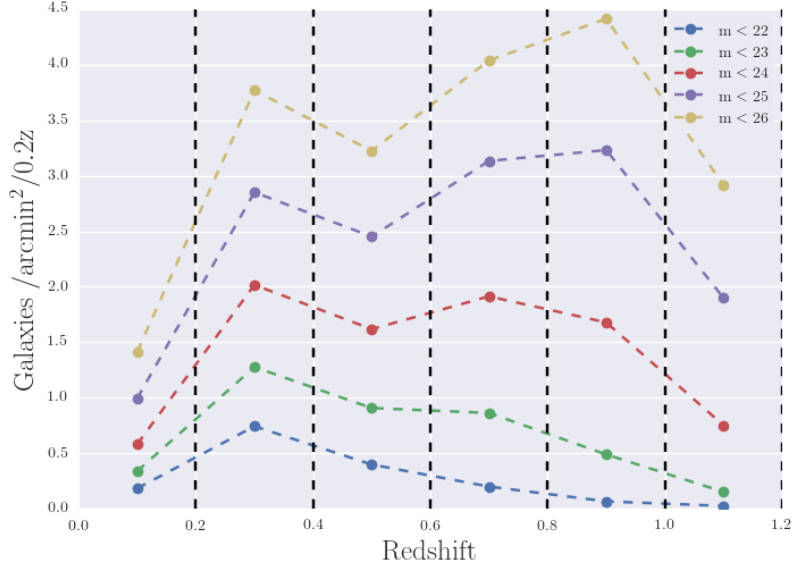


FIGURE 3.1: Galaxies per arcmin^2 in redshift bins of $0.2z$ for different magnitudes. We show the selection for different magnitudes to compare the amount of objects we expect to see with our data (CFHT and INT) with comparison to deeper data such as data obtained with HST. Around $z = 0.3$ we find the peak for the number of galaxies so it is the redshift that is most likely to contain galaxies that could be seen in our data

As a reference, we note that in the COSMOS catalogue (2017), the depths (measured flux in a 3 arc-second aperture) of the CFHT and HST data in the AB magnitude

are ~ 24 and ~ 26 respectively as seen in Figure [3.2]. The conversion from the AB magnitude to the Johnson's system is quite simple: $r = r(\text{AB}) + 0.226$ so using this reference is valid for our experiment.

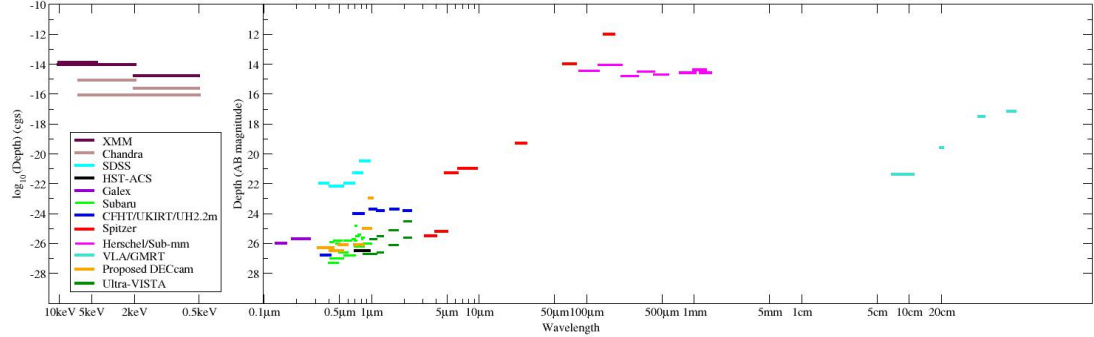


FIGURE 3.2: Depth of the different contributions to the COSMOS catalogue (AB magnitude). Source: [Cosmos 2017](#).

For the depth of our data we then expect some background galaxies lensed by the BCGs and for which we can measure the Einstein ring, although the number is small. The depth of the CFHT data is as deep as $m \sim 24$ but Hubble Space Telescope could see objects with $m \sim 26$ so it should be able to see a lot more objects that have been lensed.

This result is a first suggestion that within the inner region of the galaxy clusters, there must be lensed objects in the form of arcs or multiple images that we could be able to see with our sample making a careful subtraction of the BCG light, and we should be able to see some of these objects with the depth of our data. Now we must answer the question regarding the scales in which the stellar content (associated to the extracted light from the BCG) is relevant.

3.2 Experiment two: DM to stellar ratio

We first need to take into consideration is the density profile that we will use for our calculation of the fraction of DM and stellar light. The first usual approach for the density profile of the gravitational lens is an isothermal sphere (see Appendix), although in reality, the density profile and lensing properties of galaxies is a bit more complicated than the assumption of a SIS (singular isothermal sphere), so we need to take into account more complex but elaborate profiles such as the NFW ([Navarro, Frenk & White 1996](#)) which is an approximation to the equilibrium configuration of dark matter produced in N-body simulations of collisionless dark matter particles (see Appendix for the formalism of the NFW and its lensing equations).

So for our second experiment proposed at the beginning of the chapter, we will use the galaxy cluster Abell 1068, located at a distance of $z = 0.138$ with a reported mass of $M_{200} = 4.3 \times 10^{14} M_\odot$ ([Van der Burg et al. 2015](#)) and calculate its NFW dark matter halo profile (since galaxy clusters are known to be dominated by their dark matter content) and at the same time we calculate its stellar mass profile using the de Vaucouleurs surface brightness profile by [de Vaucouleurs \(1948\)](#) which is a specific case of a Sersic's more general profile. This allows us to compare the contribution of stars in comparison to dark matter and thus see in which scales the DM mass becomes dominant thus making it more difficult to constrain the stellar content of the bright galaxy.

The concentration parameter for the NFW profile of this cluster is $c = 4.46$ (using Figure [1] in the Appendix). The critical density is $212 M_\odot/\text{kpc}^3$. The Hubble parameter at $z = 0.138$ is $H(z) = 85.6$. For an effective radius of $R_e = 73.7 \text{ kpc}$ we get a characteristic radius of $r_{1/2} = 307.1 \text{ kpc}$.

For the stellar content of the cluster we can use de Vaucouleurs law for the surface brightness distribution in giant elliptical galaxies which is:

$$I(R) = I_e e^{-b[(R/R_e)^{1/4}-1]} \quad (3.1)$$

where $b = 7.67$ and I_e is the effective brightness which is basically the brightness at the effective radius R_e

For constant mass-to-light-ratio we have $\Sigma_*(R) = \Upsilon I(R)$ ([Lokas & Mamon 2001](#)) where $I(R) \approx 10^7 M_\odot/\text{kpc}^2$ was found by fitting the surface brightness with **GALFIT** (as will be discussed in the next chapter). The mass to light ratio for a Salpeter IMF is $\Upsilon \approx 4$ so the stellar mass profile can be easily calculated with $\Sigma_*(R) = 4I(R)$. The bolometric luminosity of Abell 1068 is 10^{44} erg/s that in solar luminosities is $1.9 \times 10^{12} L_\odot$, this gives an effective brightness of $0.962 \times 10^7 M_\odot/\text{kpc}^2$.

Hence we have the surface mass density for both the stellar content and the NFW profile, as shown in Figure [3.3].

But we are interested in the enclosed mass which can be found by integrating the surface densities. For the DM halo:

$$M(R) = 2\pi \int_0^R R\Sigma(R)dR \quad (3.2)$$

We can recover the luminosity by integrating the surface brightness profile accordingly:

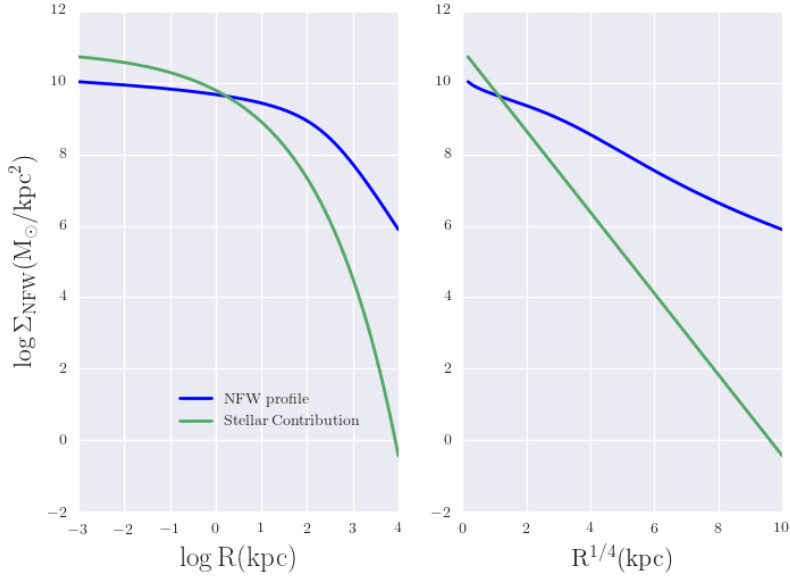


FIGURE 3.3: Surface mass density profiles in logarithmic and $R^{1/4}$ scale for the NFW profile and the stellar component.

$$L = 2\pi \int_0^R RI(R)dR \quad (3.3)$$

Let's introduce the dependence on different IMFs, mainly Salpeter, Chabrier and Kroupa. Salpeter initial mass function is of the form $n(M) \propto M^{-2.3}$ and implies that more low-mass stars and a higher mass-to-light ratio so for massive galaxies Salpeter is a good IMF.

In the R-band the scaling between the three IMFs is $\Upsilon_{\text{Krou}} \approx 0.67 \Upsilon_{\text{Salp}}$ for Kroupa and $\Upsilon_{\text{Chabrier}} \approx 0.63 \Upsilon_{\text{Salp}}$ for Chabrier. The systematic variation of the IMF in early-type galaxies can be seen in Figure [2] from the Appendix. The integration for these different IMFs give a value that is comparable to the one found using Faber-Jackson relation which is $L = \Upsilon \times \sigma^4$.

IMF/Method	Mass (M_\odot)
Salpeter	4.82×10^{12}
Kroupa	3.13×10^{12}
Chabrier	3.03×10^{12}
Faber-Jackson	2.2×10^{12}
DM Halo	4.63×10^{14}

The value found for the enclosed mass for the NFW profile is similar to the one found by [Sifon et al. \(2015\)](#) of $4.3 \times 10^{14} \text{ M}_\odot$.

Now let's analyse the radial profiles of these enclosed masses since it is the plot that shows what radial scale we need to probe. We calculate this profiles using equations [5], [7], and [9] from the NFW profile formalism included in the Appendix. The enclosed mass profile for dark matter and stellar matter for the three chosen IMFs (Chabrier, Kroupa, Salpeter) is shown in Figure [3.4].

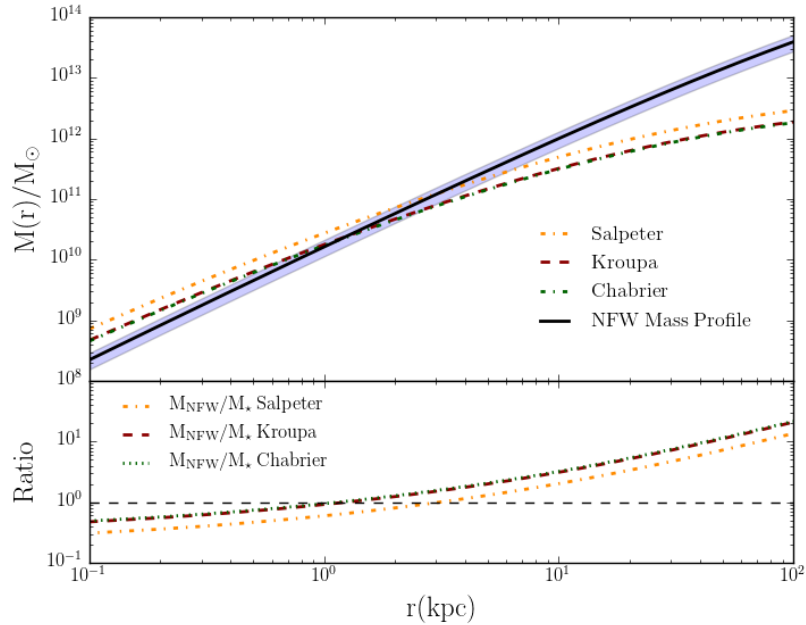


FIGURE 3.4: Top panel: Enclosed mass in DM and stellar content for the chosen IMFs for the galaxy cluster ABELL1068. Bottom panel: DM to stellar mass ratio. Note that the two contributions overlap around 1.5 kpc, that is, the very inner region of the galaxy cluster.

This result suggests that it is very difficult to make a detailed study if the stellar content of the BCG because the gravitational lensing associated to it would be mostly caused by the dark matter component at almost all scales. The stellar content is only dominant in the innermost region, quite far from the Einstein radius which is constrained by the total enclosed mass (dark matter and stars).

It is then useful to study cases in which the lens system is an elliptical galaxy following its own dark matter halo and not inside the potential well of a galaxy cluster in the case of the BCG. If we now do the calculations for a galaxy with a characteristic radius of $r_s = 25.2$ kpc and concentration parameter $c = 7.94$ we get:

IMF/Method	Mass (M_\odot)
Salpeter	2.62×10^{11}
Kroupa	1.70×10^{11}
Chabrier	1.6×10^{11}
DM Halo	3.3×10^{12}

And the radial profiles in the case of the galaxy are shown in Figure [3.5], where the overlapping happens in a larger radius.

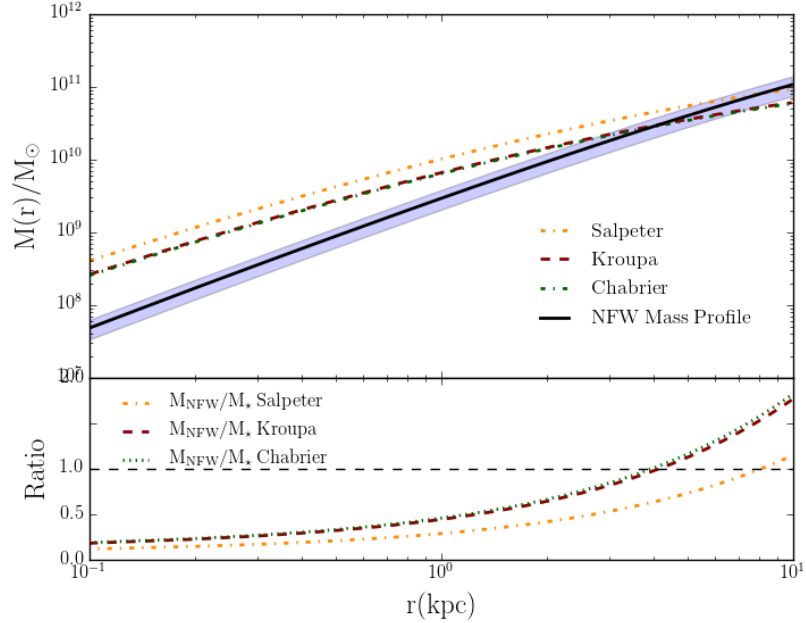


FIGURE 3.5: Top panel: Enclosed mass in DM and stellar content for the chosen IMFs for an early type galaxy. Bottom panel: DM to stellar mass ratio. The two contributions overlap around 3 kpc, further from the center than in the case of the galaxy cluster.

Our result is in good concordance with the analysis made by Sonnenfeld et al. (2012) in the system SDSSJ0946+1006, also known as the “Jackpot”. The overlapping of both contributions is around 3 kpc which is a larger radius than the one calculated for a BCG, (see Figure [3.6] for his results). The values for Sonnenfeld’s galaxy are $z = 0.222$, $c = 10^{0.9} = 7.9428$, $\delta_c = 25644.5$, $M_\star = 5.5 \times 10^{11} M_\odot$.

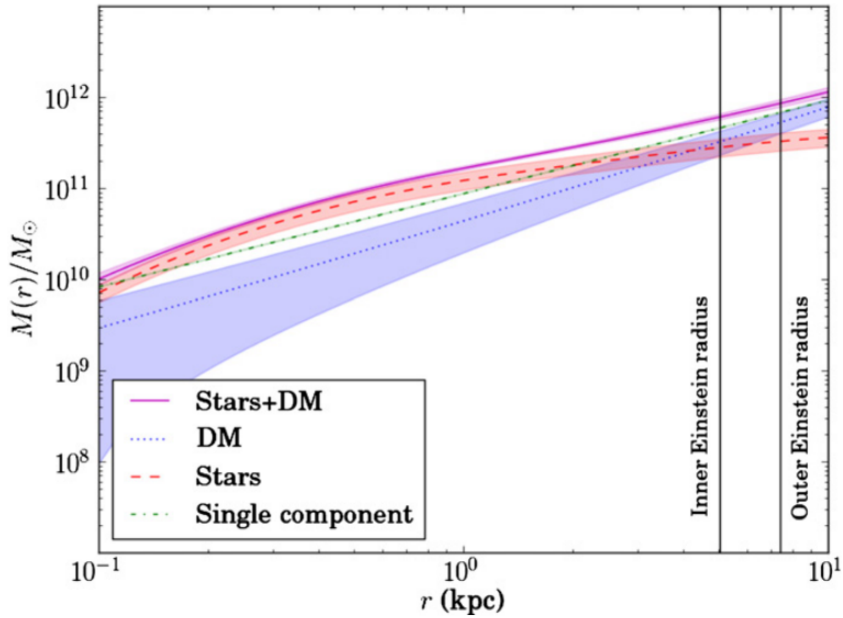


FIGURE 3.6: Mass profile for dark matter and stellar content for the lens system SDSSJ0946+1006 by Sonnenfeld et al. (2012). The overlapping of DM and stellar content is in good agreement with our calculations.

This first results mean that the proper determination of the light of the BCG (and thus tracking their formation history through an accurate determination of their IMFs) is harder to do in the inner region of galaxy clusters than it is in early type galaxies in different spatial locations. Dark matter seems to be the overwhelming dominant contribution in the bright galaxies even in the inner regions.

3.3 Experiment three: Einstein Radius

Our third experiment is another way to constrain the relevant scales in which we might expect to see lensed objects. This is done by using the lensing equations to find the Einstein radius in every case (for theoretical background objects located at different redshifts). Calculating the location of the Einstein rings is important because it is around their radial distance from the center of the BCGs that we expect to find arcs or multiple images of background objects, as displayed in Figure [3.7].

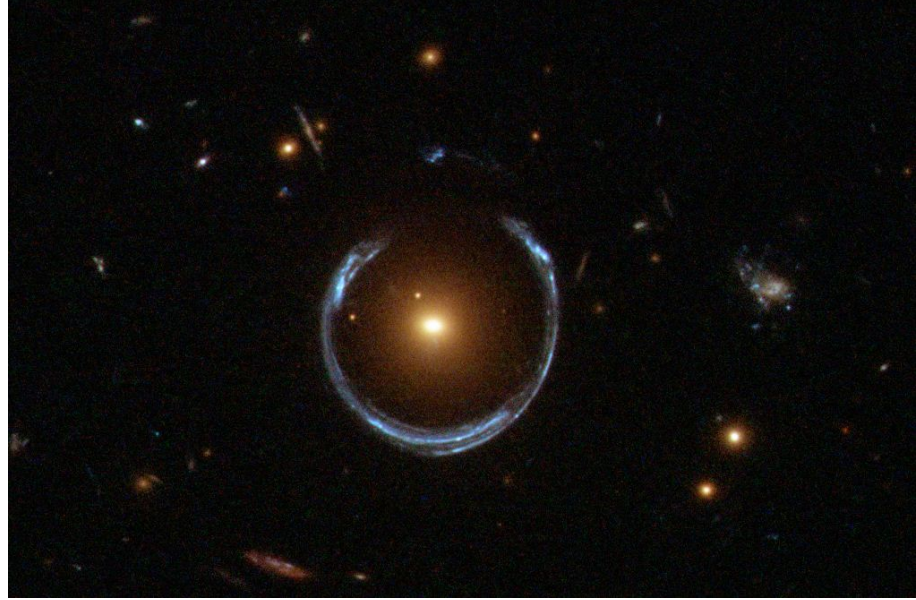


FIGURE 3.7: Einstein Ring in LRG 3-757 obtained by the Hubble Space Telescope. The distortion produced by the foreground galaxy ($z = 0.4457$) is such that the light of the background galaxy ($z = 2.379$) is stretched along the Einstein radius as well as being magnified.

Image from Wikipedia.

Since we are interested in having an accurate estimate of the Einstein radius for objects whose redshift is unknown to us, we use a range of redshifts $0.1 < z < 1$ and use the NFW density profile (see Appendix) to compute some quantities that would lead us to the radial distances of the Einstein rings such as the reduced shear and magnification (introduced in Chapter 2). Again, we display the results for the cluster Abell 1068.

The reduced shear for background objects at different redshifts is shown in Figure [3.8] as computed by equation [2.18] and also equations [7] and [10] from the Appendix. The radius in which the reduced shear diverges is where the Einstein radius would be located for each of the background objects at the different given redshifts.

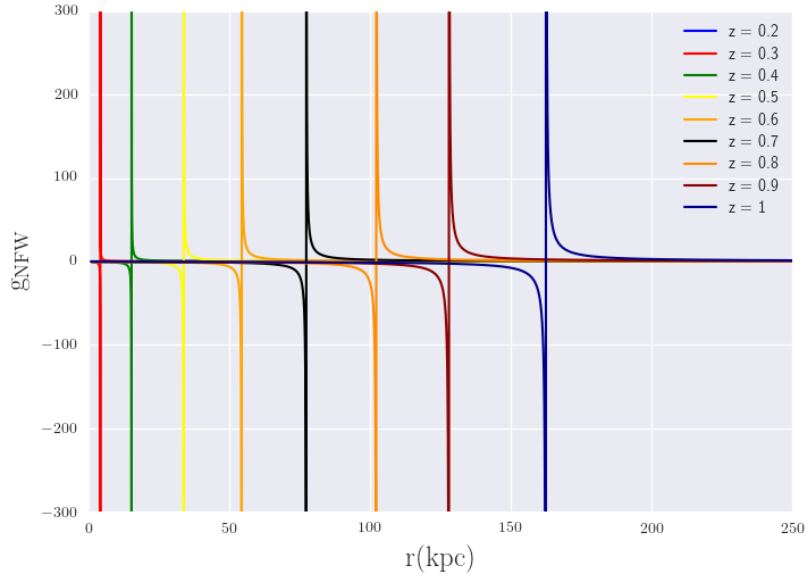


FIGURE 3.8: Reduced shear radial profile for different redshifts for Abell 1068. The divergence occurs in the location of the Einstein ring.

Another useful way to constrain the Einstein radius is through the magnification given by equation [2.19] and equations [7] and [10] from the Appendix.

Figure [3.9] shows the magnification. The infinite magnification happens in the Einstein radius so this is also a useful plot for the radial scales in which we might expect to find lensed galaxies.

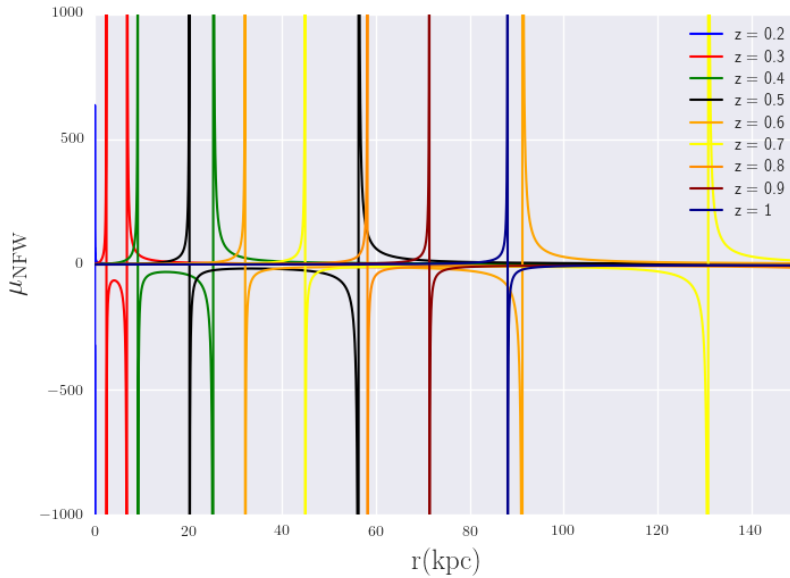


FIGURE 3.9: Magnification radial profile for various redshifts for Abell 1068. Divergence occurs in the location of the Einstein ring.

Taking into account the COSMOS catalogue experiment, and the plots for the reduced shear and the magnification, we would expect to find at least 1 or 2 lensed galaxies near a radial distance from the center of about 15 kpc, although we know that the enclosed mass at this range is already mostly dominated by the DM halo.

Chapter 4

Data and analysis

For this project we make use of good quality deep data of galaxy clusters observed with the MegaCam wide field imager on the CFHT (Canada-France-Hawaii Telescope). The cluster sample consisted of 101 clusters within the range of redshifts from $0.05 < z < 0.55$. The full description of this survey can be found in [Sand et al. \(2011\)](#)

58 clusters from the MENEACS (Multi-Epoch Nearby Cluster Survey). The MENEACS clusters represent all clusters in the BAX X-ray cluster database that are observable for the CFHT and this part of the data is in the g and r bands. We also make use of the INT data of the same cluster in the i and U bands.

After filtering out some of the clusters because of a very complex and crowded central region or just not good quality we used 30 clusters for the final studies and paid special attention to 10, marked with * in Table [4.1].

The original images have dimensions of [20000:20000] pixels but since our relevant region is the center of the cluster where the BCG is located, we cut the images with dimension of [1000,1000] for the color analysis and [4000:4000] to characterize the colors and discriminate between cluster and non-cluster members. The pixel scale for CFHT is 0.185 arcsec/pix and 0.33 arcsec/pix for the INT data so the proper conversion must be done to match them accordingly.

Cluster	z	$\sigma(km/s)$	$d(Mpc)$	$\theta_E(^{\circ})$
A1033	0.126	762	540	14.6155
A1068*	0.138	740	591.4	13.5945
A1132	0.136	727	582.9	13.1515
A119*	0.044	875	188.6	21.0798
A1413*	0.143	881	612.9	19.1569
A1650	0.084	720	360	13.6758
A1651	0.085	903	364.3	21.4876
A1795	0.062	778	265.7	16.3514
A2029*	0.077	1152	330	35.2776
A2050	0.118	854	505.7	18.5258
A2055	0.102	697	437.1	12.5642
A2064	0.108	675	462.9	11.7048
A2065*	0.073	1095	312.9	32.0110
A2069	0.116	966	497.1	23.7574
A2142*	0.091	1086	390	30.8756
A2319*	0.056	1101	240	32.9563
A2420	0.085	800	364.3	16.8653
A2440	0.091	766	390	15.3608
A2597	0.085	682	364.3	12.2569
A2627	0.126	800	540	16.1096
A2703	0.114	800	488.6	16.3307
A399	0.072	800	308.6	17.1049
A553	0.066	800	282.9	17.2155
A655*	0.127	800	544.3	16.0911
A754*	0.054	800	231.4	17.4367
A763	0.085	800	364.3	16.8653
A795	0.136	800	582.9	15.9252
A85*	0.055	800	235.7	17.4182
A961	0.124	800	531.4	16.1464
A990	0.144	800	617.1	15.7778

TABLE 4.1: Abell clusters used in this work. Marked with * the chosen clusters with the most promising features. From left to right: Name of the cluster, redshift, velocity dispersions from [Sifon et al. \(2012\)](#), distance in Mpc and Einstein Ring using a single isothermal sphere as first approximation.

The INT images were obtained using multiple exposures so it was necessary to make a mosaic of them using SWARP [Bertin et al. \(2002\)](#), so at the end we had the data of the clusters in the bands g, r, U, i with the same spatial scale. The first step in the removal of

the light from the BCG was constructing a mask file (segmentation file) to only extract the desired galaxy, this was done using **SEXTRACTOR** ([Bertin & Arnouts 1996](#)).

The procedure is the following: **SEXTRACTOR** identifies the bright objects and extracts them while doing aperture photometry on them, the user can choose to obtain an examination image to see the extracted objects (that in our case would be the segmentation file). **SEXTRACTOR** labels each of the extracted regions with growing numbers where 1 is the brightest object (in most cases the BCG) so we can use python scripts to modify the segmentation file to mask only the galaxies but not the BCG which we want to fit properly. Figure [4.1] shows the original segmentation image and the one where the BCG light has been removed so that it won't be masked once we fit the light of the BCG (cluster Abell 754).

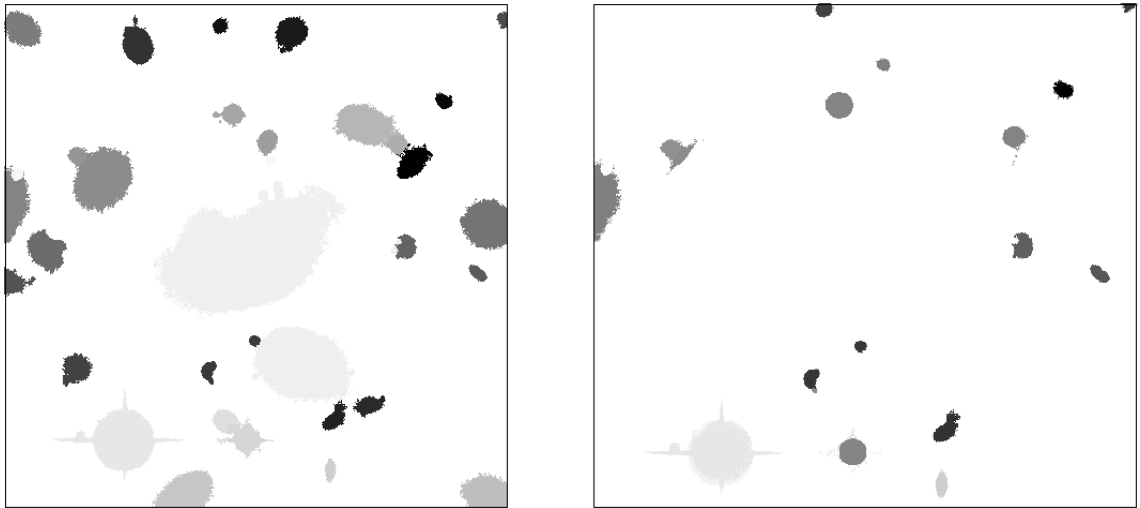


FIGURE 4.1: Segmentation images produced by **SEXTRACTOR** and used as mask files for the galfit extraction on the cluster Abell 754. Left panel is the original mask with all the bright objects. Right panel is the mask after the subtraction of the regions surrounding the cluster galaxies to be fitted with **GALFIT**. The colors are inverted for an easier visualization of the image. The fainter regions are actually the most luminous objects because **GALFIT** assigns increasing numbers starting from the brightest one, that is the BCG in this case.

Now, once the mask file is ready we can do the subtraction of the BCG light using **GALFIT** ([Peng et al. 2002](#)) which fits two dimensional profiles of galaxies (with different shapes and features). The first subtraction for most of our target clusters was done fitting a Sersic's profile with $n = 4$ which is de Vaucouleurs profile. Although in all cases some parameters such as the n index, the effective radius, Fourier and bending modes were to be changed and modified accordingly. A first run of **GALFIT** gives us a rough idea of the true position of the center of the BCG so we can set this values in a second run for each cluster.

We use the segmentation masks given by **SEXTRACTOR** to mask bright objects in the fitting of the BCG but in some cases it was necessary to do the fitting of many objects

(not only the BCG). The best results were given when we also masked the innermost region of the BCG (the size of the seeing) so the fitting will put more weight in the rest of the profile, thus reducing most of the light that hides the background objects.

The power of **GALFIT** lies in the fact that it allows for different shape fitting through Fourier and bending modes. These parameters (C_0 , B_1 , B_2 , F_1 , F_2 , etc.) are hidden from the user unless he/she explicitly requests them. These can be tagged on to the end of any previous components except, of course, the PSF and the sky.

Some of the useful parameters that we used to properly fit the BCG in every case were:
 B1) Bending mode 1 (shear term), B2) Bending mode 2 (banana shape) B3) Bending mode 3 (S-shape) and for the azimuthal fourier modes F_i) Az. Fourier mode i where i can go up to a 20th Fourier mode, C0) traditional diskyness(-)/boxyness(+).

Figure [4.2] shows the original image, the fitted models and the output given by **GALFIT** for the cluster Abell 754. Note that many galaxies were fitted and many background objects can be seen near the center of the BCG.

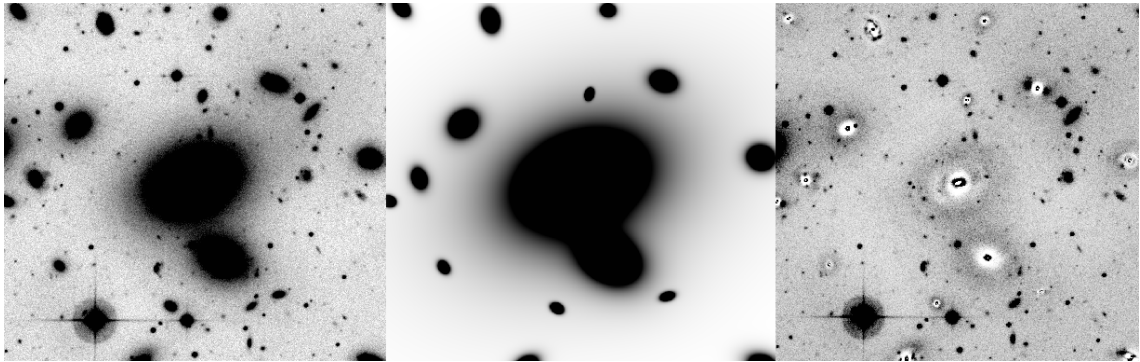


FIGURE 4.2: Galfit procedures for Abell 754. Left: Original image in “zscale” with the BCG expanding across a significant region of the central area. Middle: The models fitted by **GALFIT** for all the selected cluster galaxies. Right: Residual image after the subtraction of the model galaxies. Note that the saturated star is not in the **GALFIT** models since it is simply masked out with the segmentation image.

GALFIT can make a good estimate on the ellipticity and effective radius of the galaxies, and it performs an algorithm that integrates the brightness of every object giving a more accurate integrated magnitude than the first guess given by the user in the parameter file. The BCG’s integrated magnitudes oscillate between values of $U \sim 22$, $i \sim 18$, $g \sim 20$, $r \sim 19$.

These procedures are done over all the images and their 4 filters, which will allow us to make color images and discriminate between objects of the same color that could be lensing candidates as explained in the next section. For every cluster the images have the same spatial scale and are centered at the same exact location so we can use the same fitting models for every filter as seen in Figure [4.3]

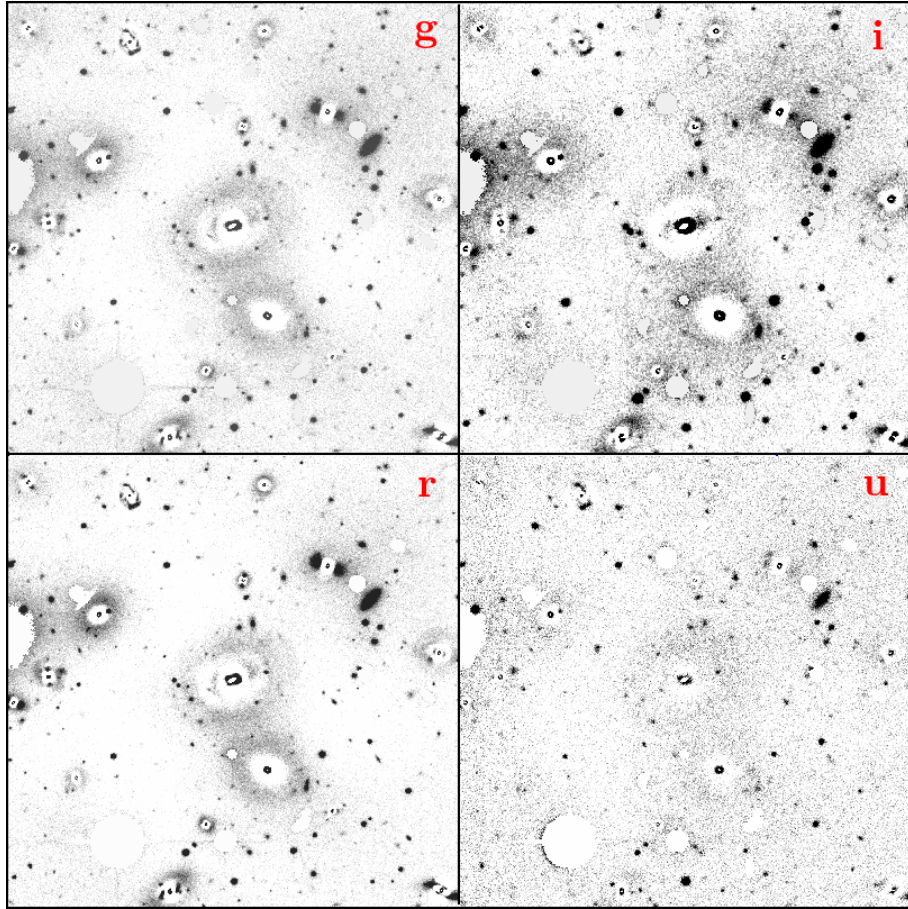


FIGURE 4.3: GALFIT results for the four available filters (g, i, r, U respectively) of Abell 754 displayed in zscale. Note that depending on the filters some objects appear to be brighter or fainter and that will play an important role in the creation of the color images and the photometric redshifts explained in the following sections.

The same procedure is applied on all the clusters. One of the most interesting targets of our sample is the cluster Abell 1413 (located at $z = 0.143$) which has a prominent arc as seen in Figure [4.4] (although this cluster lacks of the U band image).

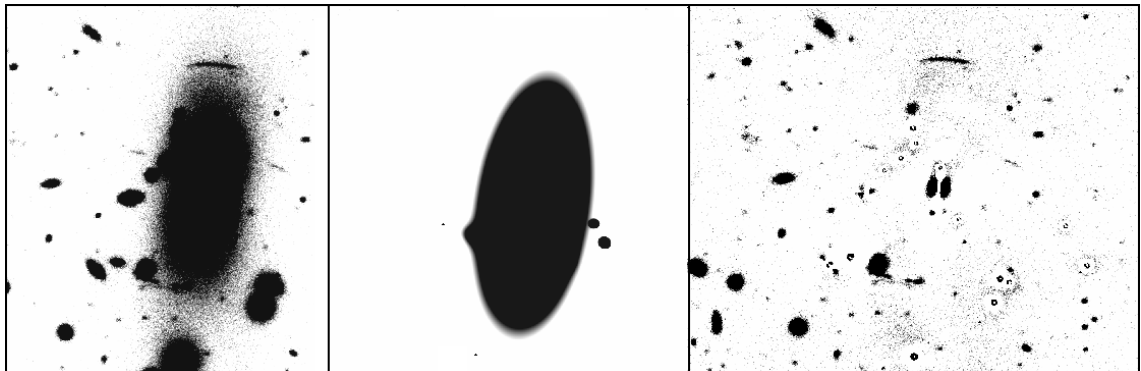


FIGURE 4.4: Galfit procedures for Abell 1413. Left: Original image in “zscale” with the BCG. Middle: The models fitted by GALFIT for all the selected cluster galaxies. Right: Residual image after the subtraction of the model galaxies. This cluster in particular has many non-cluster members so fewer objects need to be subtracted.

4.1 Color images

We use **IRAF** to make the color images using our g, r, U, i bands. Let's keep using Abell 754 which is a low redshift galaxy ($z = 0.054$) cluster with a calculated mass of $M_{200} = 9.8 \times 10^{15} M_\odot$ ([Sifon et al. 2015](#))

We made a color image of the original center of the cluster without subtracting the BCG in order to differentiate between cluster members from background galaxies and field stars. This allows us to fit only the cluster galaxies. Figure [4.5] shows the color image of the center of the cluster where we used an isothermal sphere to model the Einstein ring for an assumed distance of background objects of $z = 0.5$.

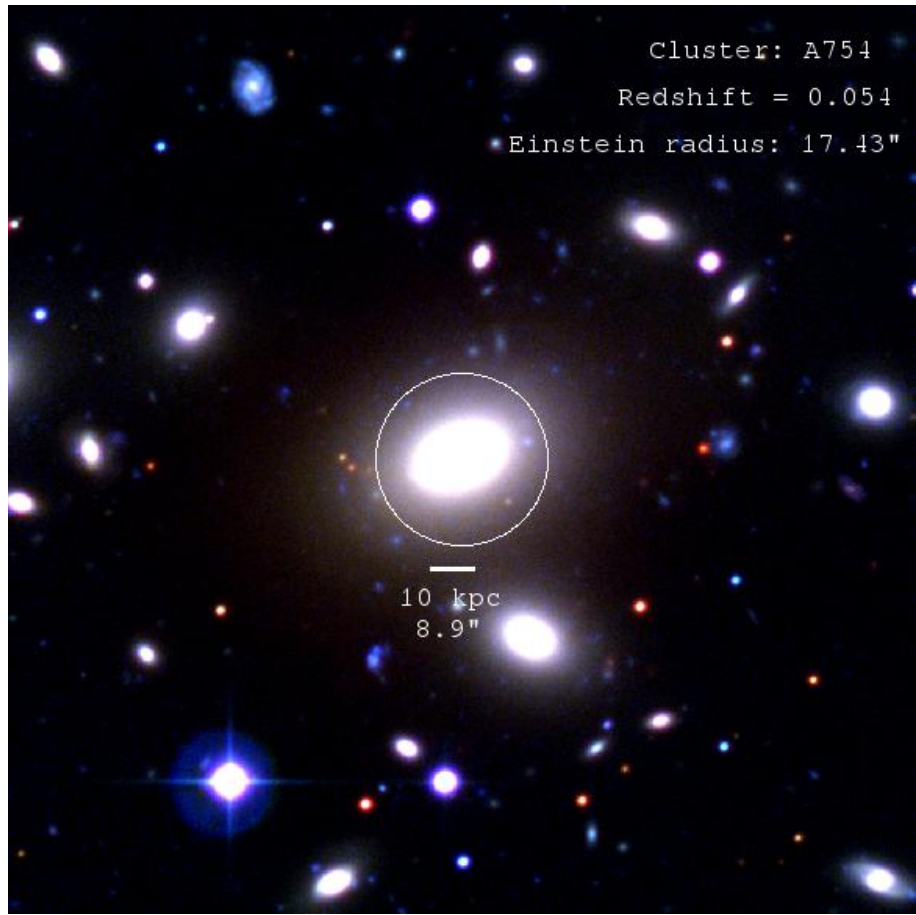


FIGURE 4.5: Color image of A754 cluster (filters i, g, U) with its Einstein radius calculated for an isothermal sphere of a background object at $z = 1$.

After choosing the galaxies that belong to the cluster by comparing their relative colors, we subtracted them using **GALFIT** and made the color image again changing the scaling values with the task **CONVERT** of **IRAF** so that we get a better color contrast to search for good candidates of lensed objects. By looking at this reduced color image, we have another visual constraint to choose the clusters in which it would be worth to do

photometric redshifts and search for objects with the same redshift in different locations around the very center of the BCG (object that has been strong lensed). Figure [4.6] displays the color image of the BCG-subtracted center of Abell 754.

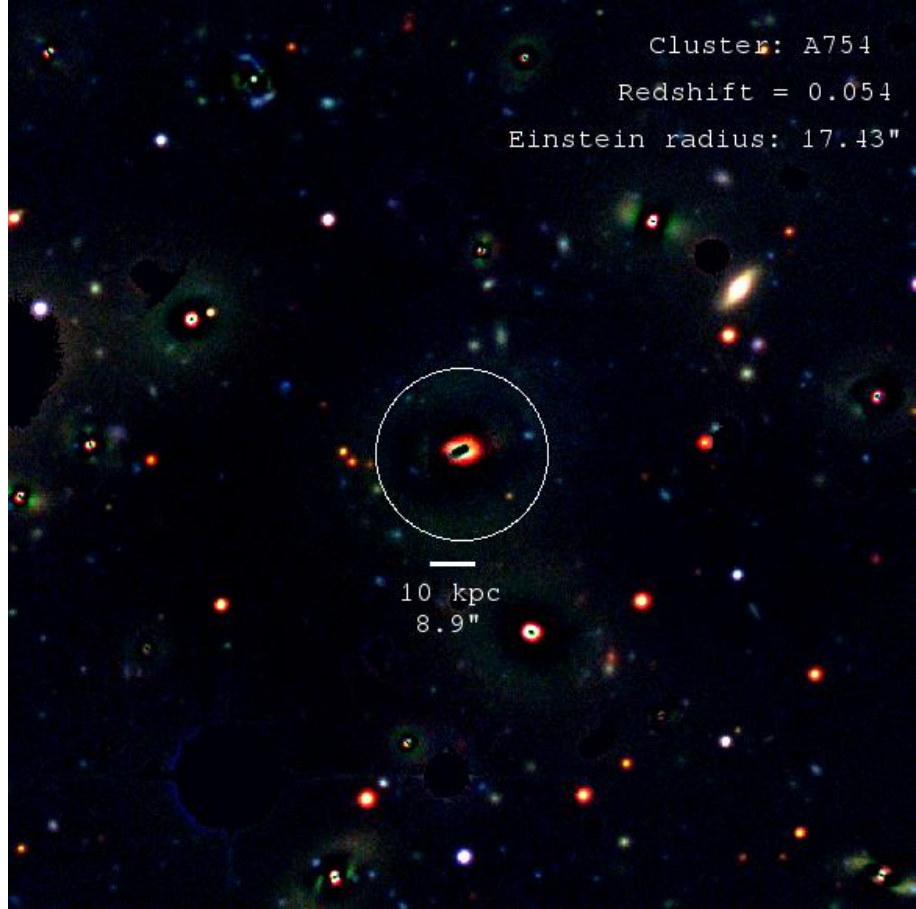


FIGURE 4.6: Color image of A754 cluster (filters i, g, U) after the subtraction of the bright cluster galaxies. Note that after the subtraction of the BCG, objects with different colors show up in the central region and close to the Einstein radius.

The subtraction of the most prominent cluster members near the BCG is very important since their light doesn't allow for searching the lensing candidates, although in some cases this is not necessary, in those cases the error is smaller since the background subtraction only depends on one component so it's not overestimated. Figure [4.7] shows the i, r, g color image of the previously mentioned cluster Abell 1413.

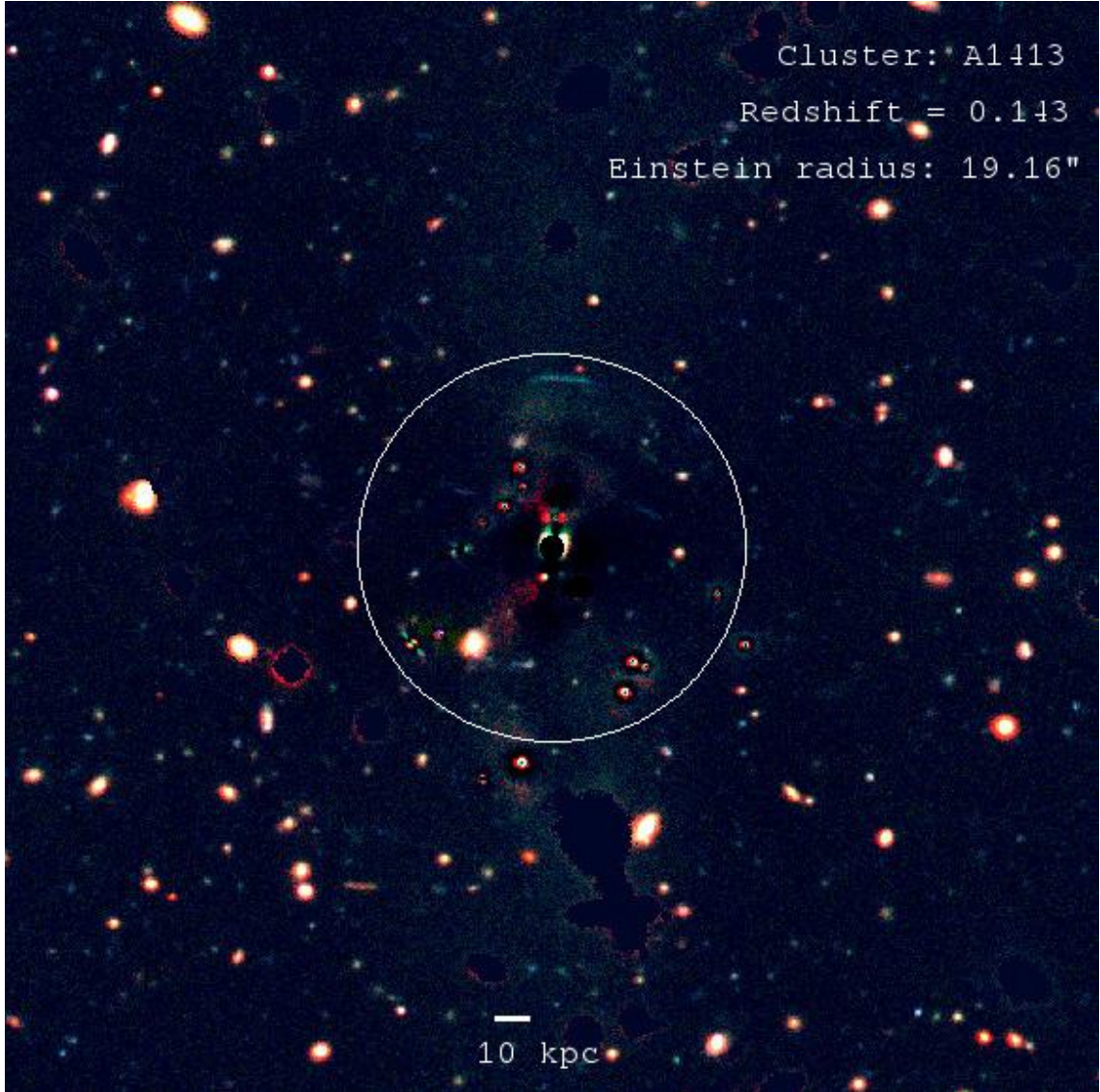


FIGURE 4.7: Einstein ring in the BCG-subtracted color image of Abell 1413. As seen in the symmetric ripples in very center of the BCG, this subtraction required the use of Fourier modes which allow for a better fitting of its brightness profile.

Because we have 4 bands we were able to make different color images to see the contrast and make combinations that would allow us to see better the very red and very blue objects, hoping to find objects with the same colors that would be good candidates for lensed objects. Figure [4.8] displays the g, r, i, r, g and i, g, U color images for three clusters (Abell 961, Abell 2703 and Abell 1033).

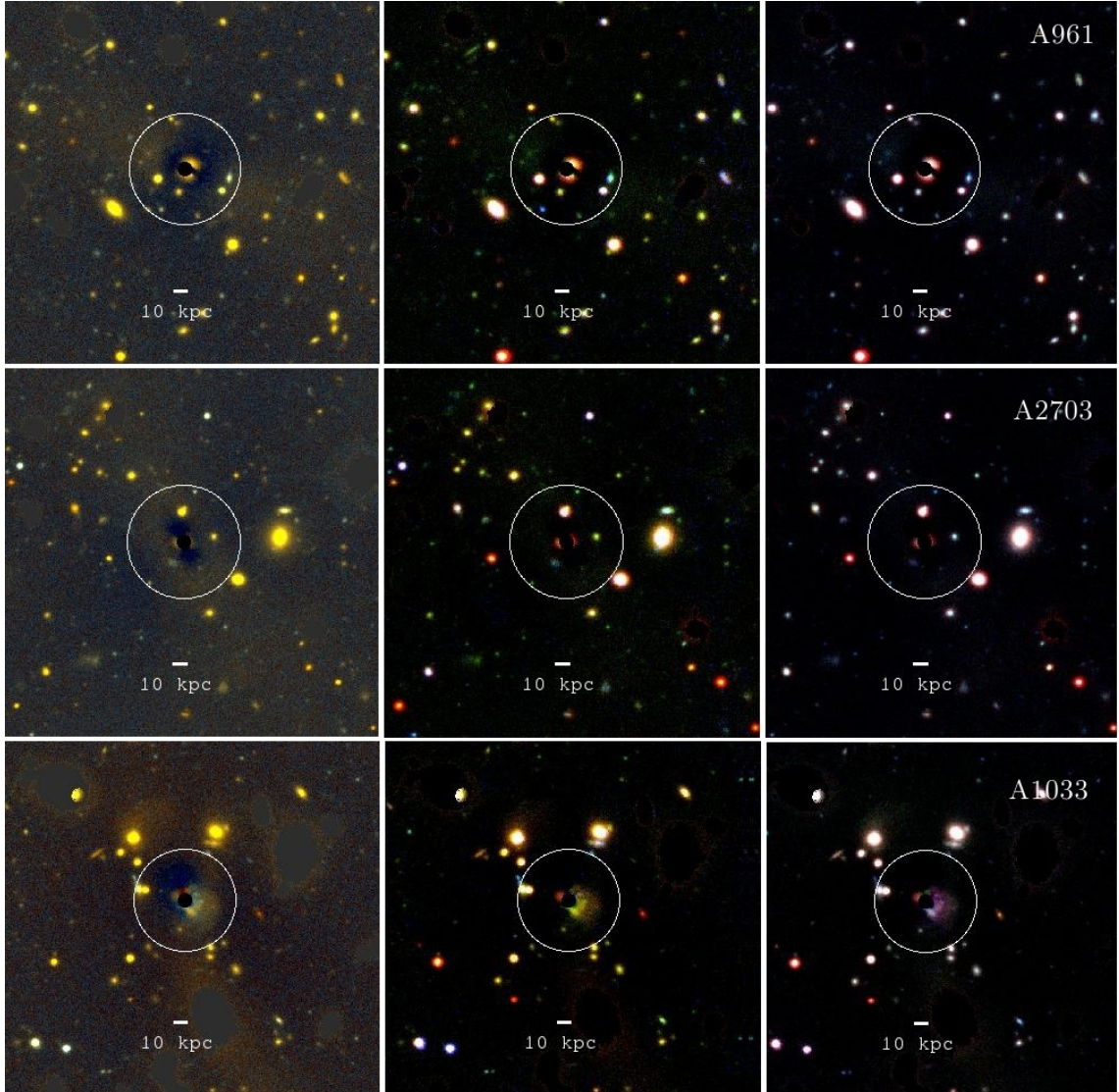


FIGURE 4.8: Different color images for different combination of the g, r, U, i filters for the clusters Abell 961, Abell 2703, Abell 1033. Left column for the images constructed only with the g and r filter, central column for i, g, r and right column for i, g, U .

4.2 Star-galaxy determination

The first step in determining the photometric redshifts is to discriminate between field stars and the galaxies of the clusters so in order to do this, we used some of the parameters found by **SEXTRACTOR** that allow us to constraint the fitted data. These are `class-star`, `flux_radius`, and `FWHM` (full width half maximum). `Class-star` uses the neural network star/galaxy of **SEXTRACTOR** that will give values close to 1 for stars and 0 for galaxies. `flux_radius`, and `FWHM` are closely related to each other and give the radius which contains half of the light of the object so it will be small for stars and bigger for extended objects.

In order to extract the same objects and make the segmentation masks for the desired objects in the different filters, we used **SEXTRACTOR** on dual mode and made aperture photometry on each of the relevant objects. Figure [4.9] shows the color magnitude diagram for Abell 754 where we used a zero point magnitude of 30.

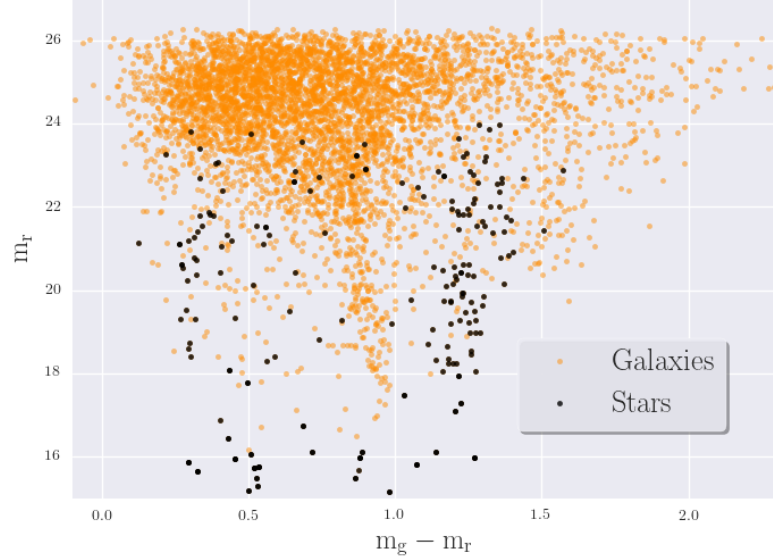


FIGURE 4.9: Color Magnitude diagram of Abell 754 with the differentiation of stars from galaxies.

We can also discriminate the stars from galaxies using the radius that contains most of the flux. Figure [4.10] shows the galaxies and stars in the mag vs Flux_rad plane.

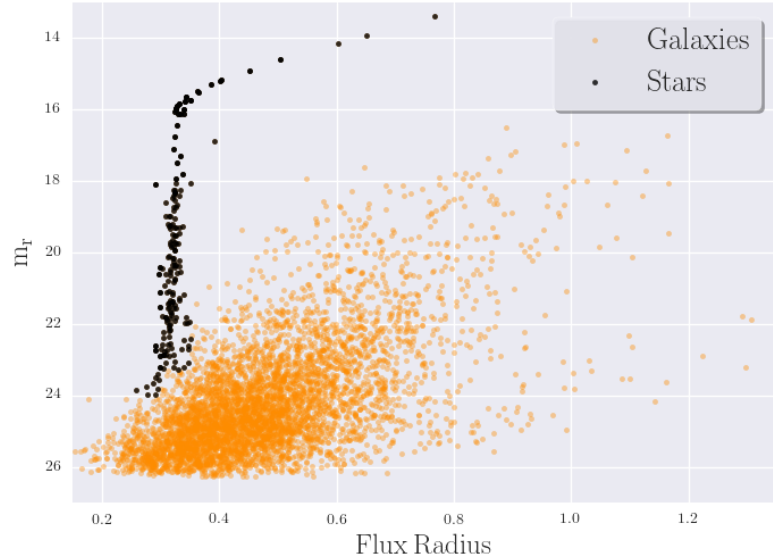


FIGURE 4.10: Magnitude vs Flux radius of Abell 754 to identify the galaxies using the criteria of their flux distribution.

4.3 Photometric Redshifts

Using multi band photometry data to get redshifts (Photometric redshifts) is not only a useful method to get redshifts of fainter objects than accessible by spectroscopy, but also because the efficiency in terms of the number of objects with redshift estimates per unit telescope time is largely increased. Given the characteristics of our data (four bands with similar depth), getting photo- z 's of the background objects after the subtraction of the BCG's could in principle help us find lensed galaxies (background objects with the same redshift could be the same galaxy located at different locations so they are good lensing candidates).

In order to calculate the photometric redshifts we must make very accurate photometry on the four bands trying to minimize the errors associated to the removal of the light from the BCG that causes the photometry methods to overestimate or underestimate the background thus corrupting the output magnitudes. As seen in Figure [4.11], the background in the vicinity of some of the objects is over removed after the subtraction of the light of the BCG, so this effect would cause objects with the same real redshift (lensed background galaxies) to have different redshifts after running the photo- z code.

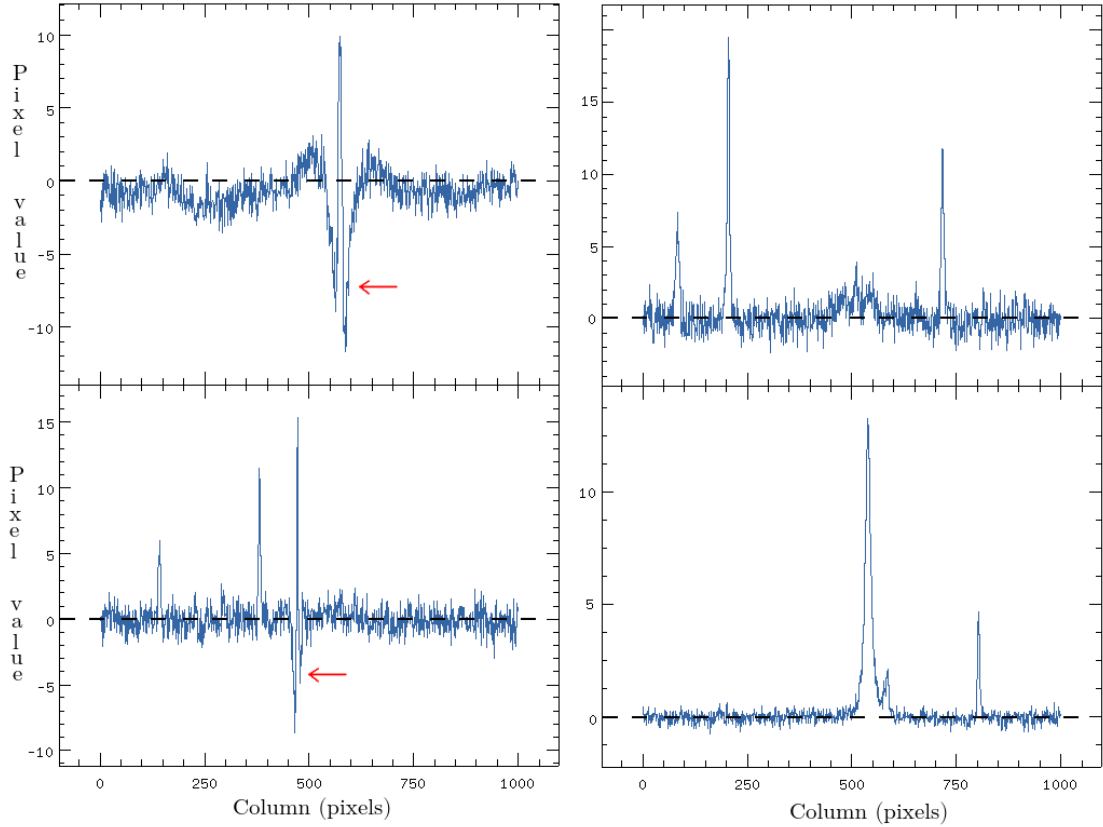


FIGURE 4.11: Horizontal cuts on cluster Abell 1068 for four random regions. On the left, objects with an overestimated background (indicated with the red arrows) where the values of the surroundings go well below zero. On the right, objects surrounded by a more accurate and smooth background.

In order to avoid this problem, we applied different methods for the photometry of the reduced data with a careful local background determination in every case. The very first approach (just for reference) was simply aperture photometry using **SEXTRACTOR** with the default parameters, the other methods were more precise and were made using the aperture photometry routines of **PHOTUTILS**. The first method is making aperture photometry with an annulus enclosing the surrounding background of every galaxy, the second method is choosing a fixed background (the mean value found with **IMSTATISTICS** of **IRAF**) and use it as the value for all the apertures, the third one is the average between the fixed background and the background value found in the annulus surrounding the objects. Figure [4.12] shows the objects on which we applied the photometry experiments for the galaxy cluster Abell 754.

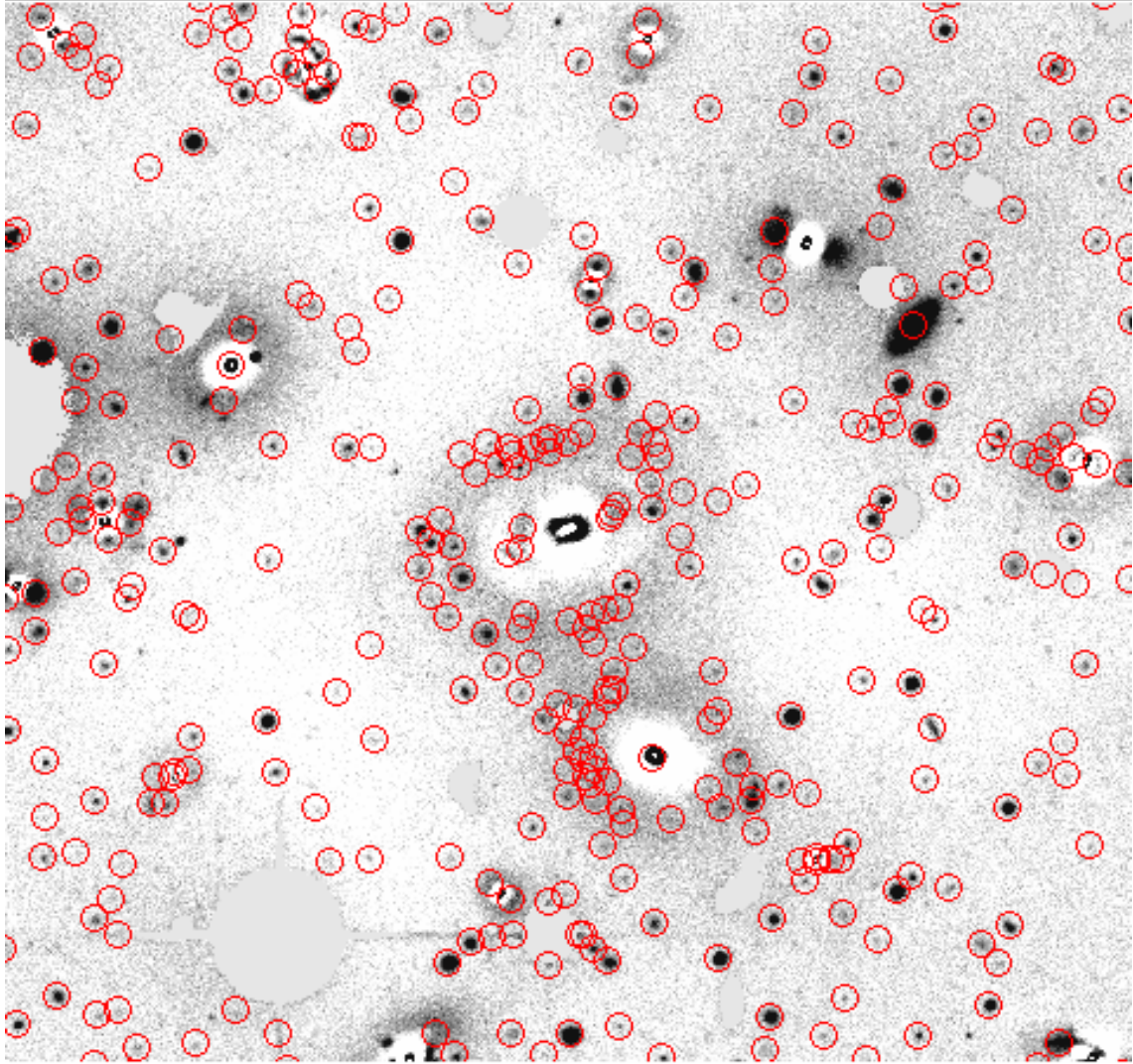


FIGURE 4.12: Apertures for the aperture photometry procedures for the core of galaxy cluster Abell 754. This is the full sample of objects without the discrimination of stars and galaxies from the cluster.

The physical coordinates of the objects were obtained with **SEXTRACTOR** since the filtering and identification of the objects is quite straight forward. Once we have obtained the magnitudes of the galaxies in our four filters, and have chosen the method that yields the most satisfactory results (in our case the average between the fixed background and the one associated to the annuli), we can measure the photometric redshift of the galaxies in the inner region of the cluster.

We use the photometric redshift code **EAZY** by Brammer et al. (2008) which uses an extensive collection of spectral energy distributions for galaxies in the range $0 < z < 4$. It basically finds discontinuities such as Lyman break (1200 Å) and the Balmer break (4000 Å) in the SED of galaxies which give a constraint on the redshift. Fortunately, the code includes library from CFHT in the *i* and *U* bands but doesn't have the filters in the

g and r bands so we used the SUBARU survey filter information to be able to compute the photometric redshifts using the four bands. The use of a r band magnitude prior allows the code to correctly calibrate the redshifts since the location of the break might be misunderstood by the code. Figure [4.13] shows our obtained photometric redshifts for the cluster Abell 754 (376 galaxies after filtering out field stars and removing the brightest galaxies that belong to the cluster) for all of our photometry experiments and compared them to the ones found by Remco Van der Burg (private communication) on a larger field for the same cluster.

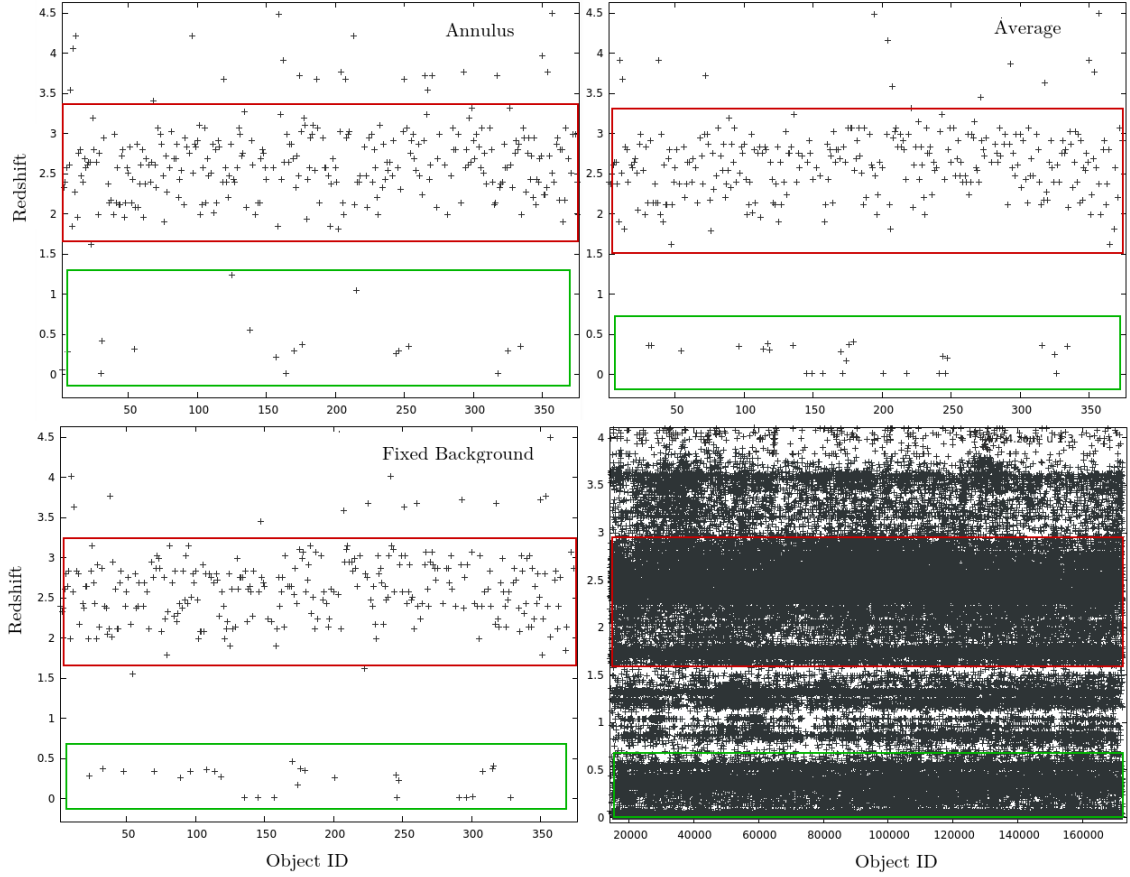


FIGURE 4.13: Photometric redshift results for Abell 754. Top left: Results for the photometry method in which the background was determined with an annulus around the objects. Bottom right: Using a fixed background (mean of the background). Top left: An average between the two other methods. Bottom left: Van der Burg’s results for the photo- z ’s for a much larger sample (188,964 objects). The red squares represent the regions of the “junk” data which we can neglect for the lensing analysis. The green squares indicate the regime of the background galaxies where we want to look for lensing candidates.

One last filter has to be applied to the data. Since the calculated redshifts should be consistent with the expected values according to the COSMOS experiment, we need to select only the galaxies that have low redshifts (they are more suitable for being lensing candidates in the sample). For this, we only select the galaxies whose photo- z ’s are in

the low regime as shown with the green squares in Figure [4.13] and use their respective ID to identify their corresponding magnitude.

Now that we have selected the magnitude in every filter for the filtered galaxies, we analyze their flux distribution by plotting their arbitrary flux against λ , taking as reference the effective wavelengths of the filters U, g, r, i , and see the shape of their distribution. If we find objects with very similar flux distributions (similar behavior in the plot), then we might check their coordinates and see whether this difference is a coincidence or they can be in fact the same object.

Figure [4.14] shows the magnitude distribution for the final filtered sample of galaxies surrounding the BCG of Abell 2064. We see that two objects present a very similar magnitude distribution so it is an interesting target to look at.

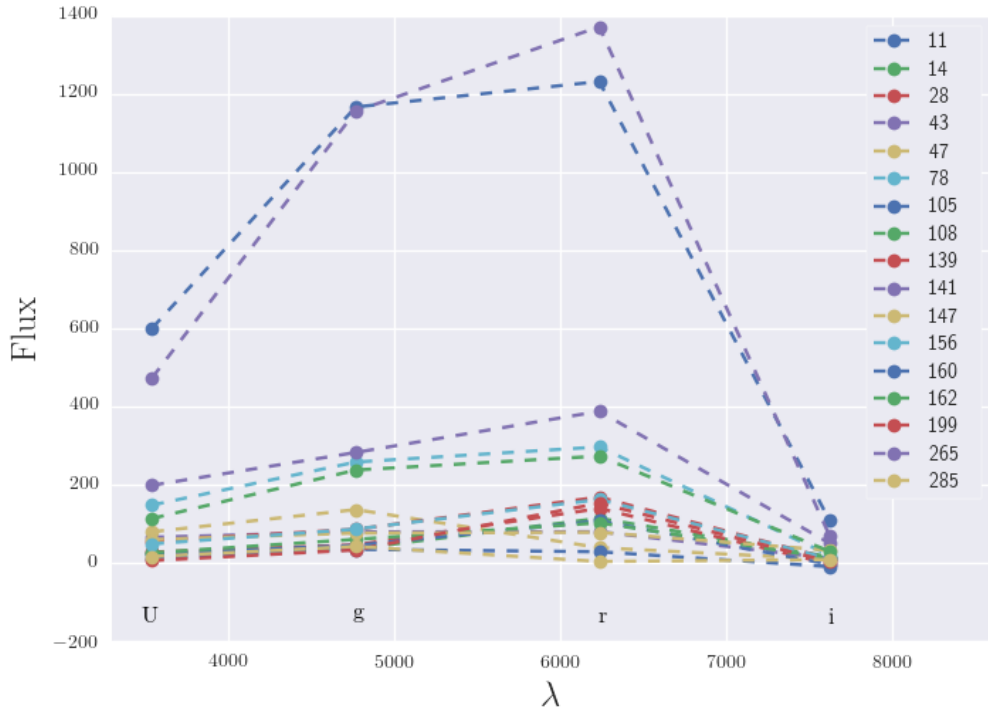


FIGURE 4.14: Magnitude distribution for galaxies with low photometric redshift and their respective ID for cluster Abell 2064. Note that the only 17 galaxies belong to the low redshift regime out of the 320 galaxies over which we ran the photo-z code.

Even though the two most prominent plots in Figure [4.14] appear to have a bad flux distribution, they are still interesting candidates since we care about the similarities between their distributions instead of how well behaved they are. Figure [4.15] shows the location of the objects that have a similar flux distribution with their corresponding ID in two different color images (i, g, u and i, r, g).

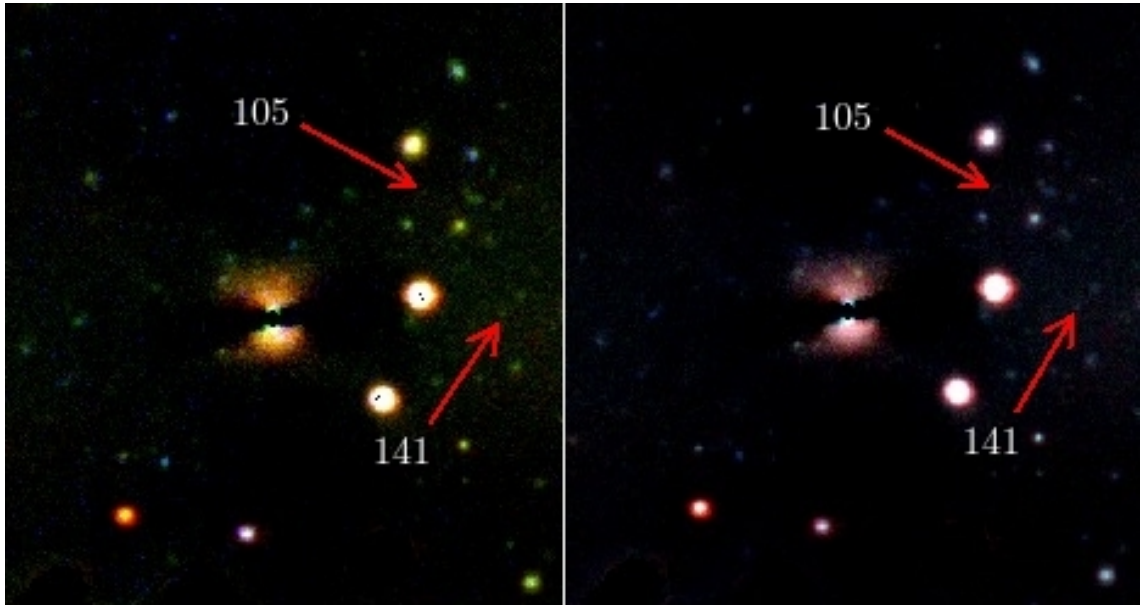


FIGURE 4.15: Lensing candidates in Abell 2064. Left: Color image made with the i, g, u filters. Right: Color image made with the i, r, g filters. Note that an inspection by eye would miss the objects because they are very faint.

In principle, both galaxies seem to have a very related flux distribution so the two points seem to be good candidates for a more precise analysis, but unfortunately the photometric redshift for both galaxies is not similar and they are very faint to give trustworthy results, specially with the U -band data so it is discarded as a good candidate.

Chapter 5

Conclusions

We don't expect too many sources in our sample data since the amount of sources that can reach the telescope with a sensitivity of $m = 23$ is rather small and the difficulty of removing the BCG can make it even harder.

The proper determination of the light of the BCG (and thus tracking their formation history through an accurate determination of their IMFs) is harder to do in the inner region of galaxy clusters than it is in early type galaxies in different spatial locations.

Dark matter seems to be the overwhelming dominant contribution in the bright galaxies even in the inner regions. It seems to be more densely packed in galaxy clusters than it is in isolated early type galaxies with their own dark matter halo.

Like Abell 1413 where the arc is clearly seen. Need U band data and do the follow up studies of the cluster.

Appendix

Isothermal Sphere

Summary of isothermal sphere:

$$\rho(r) = \frac{\sigma^2}{2\pi Gr^2} \quad (1)$$

$$\Sigma(\xi) = \frac{\sigma^2}{2G\xi} \quad (2)$$

The Einstein radius:

$$\xi_E = 4\pi \left(\frac{\sigma}{c}\right)^2 \frac{D_{ds}}{D_s} \quad (3)$$

NFW profile formalism

The NFW density profile is

$$\rho(r) = \frac{\delta_c \rho_c}{(r/r_s)(1+r/r_s)^2} \quad (4)$$

where the characteristic over density (dimensionless quantity) is given by:

$$\delta_c = \frac{200}{3} \frac{c^3}{\ln(1+c) - c/(1+c)} \quad (5)$$

The mass of an NFW halo contained within a radius of r_{200} is:

$$M_{200} = M(r_{200}) = \frac{800\pi}{3} \rho_c r_{200}^3 = \frac{800\pi}{3} \frac{\bar{\rho}(z)}{\Omega(z)} r_{200}^3 \quad (6)$$

The concentration parameter c is strongly correlated with Hubble type, $c = 2.6$ separating early from late-type galaxies. Those galaxies with concentration indices $c > 2.6$ are early-type galaxies reflecting the fact that the light is more concentrated towards their centres, its formal definition in terms of the virial and characteristic radius is $c = r_{200}/r_s$.

[Dutton & Maccio \(2014\)](#) (in continuation of previous studies such as [Muñoz Cuartas et al. 2010](#)), made simulations of halo masses from dwarf galaxies to galaxy clusters

and find constraints on the concentration parameter for different redshifts, the relation between the concentration parameter with redshift and virial mass is shown in Figure [1].

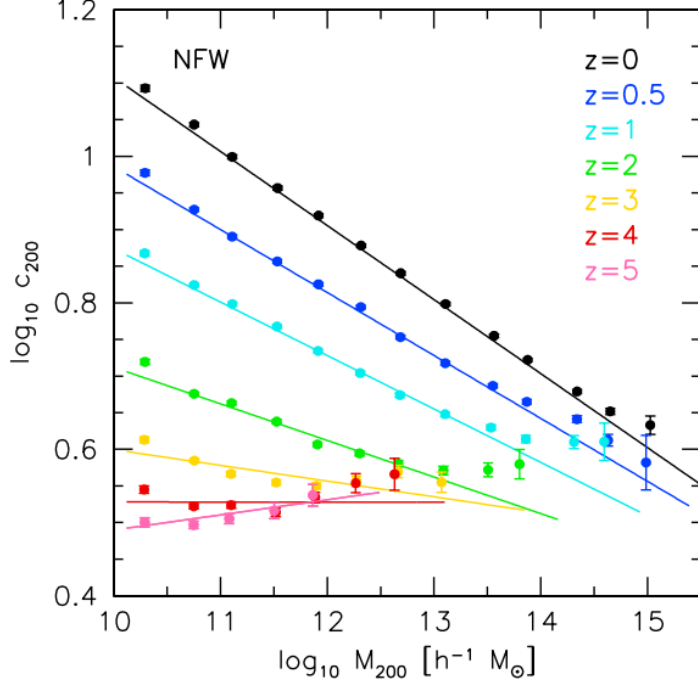


FIGURE 1: Evolution of the concentration mass relation, by [Dutton & Maccio \(2014\)](#).

The surface mass density in the NFW profile ([Wright & Brainerd, 1999](#)) is given by:

$$\Sigma_{\text{NFW}}(x) = \begin{cases} \frac{2r_s\delta_c\rho_c}{(x^2-1)} \left[1 - \frac{2}{\sqrt{1-x^2}} \operatorname{arctanh} \sqrt{\frac{1-x}{1+x}} \right] & (x < 1) \\ \frac{2r_s\delta_c\rho_c}{3} & (x = 1) \\ \frac{2r_s\delta_c\rho_c}{(x^2-1)} \left[1 - \frac{2}{\sqrt{x^2-1}} \operatorname{arctan} \sqrt{\frac{x-1}{1+x}} \right] & (x > 1) \end{cases} \quad (7)$$

so from the critical density:

$$\rho_c = \frac{3H^2(z)}{8\pi G} \quad (8)$$

$$H(z) = H_0(1 + \Omega z)^{3/2}$$

But we are more interested in the enclosed mass which can be done by integrating the surface mass density:

$$M(R) = \int_0^R 2\pi R \Sigma(R) dR \quad (9)$$

The radial dependence on the shear is:

$$\gamma_{\text{NFW}}(x) = \begin{cases} \frac{r_s \delta_c \rho_c}{\Sigma_c} g_{<}(x) & (x < 1) \\ \frac{r_s \delta_c \rho_c}{\Sigma_c} \left[\frac{10}{3} + 4 \ln \left(\frac{1}{2} \right) \right] & (x = 1) \\ \frac{r_s \delta_c \rho_c}{\Sigma_c} g_{>}(x) & (x > 1) \end{cases} \quad (10)$$

where:

$$g_{<}(x) = \frac{8 \operatorname{arctanh} \sqrt{\frac{1-x}{1+x}}}{x^2 \sqrt{1-x^2}} + \frac{4}{x^2} \ln \left(\frac{x}{2} \right) - \frac{2}{(x^2-1)} + \frac{4 \operatorname{arctanh} \sqrt{\frac{1-x}{1+x}}}{(x^2-1)(1-x^2)^{1/2}} \quad (11)$$

$$g_{<}(x) = \frac{8 \operatorname{arctan} \sqrt{\frac{x-1}{1+x}}}{x^2 \sqrt{x^2-1}} + \frac{4}{x^2} \ln \left(\frac{x}{2} \right) - \frac{2}{(x^2-1)} + \frac{4 \operatorname{arctan} \sqrt{\frac{x-1}{1+x}}}{(x^2-1)^{3/2}} \quad (12)$$

For reference, Figure [2] shows strong systematic variation of the IMF in early-type galaxies as a function of their stellar mass-to-light ratio, producing differences up to a factor of three in mass by [Cappellari et al. \(2012\)](#)

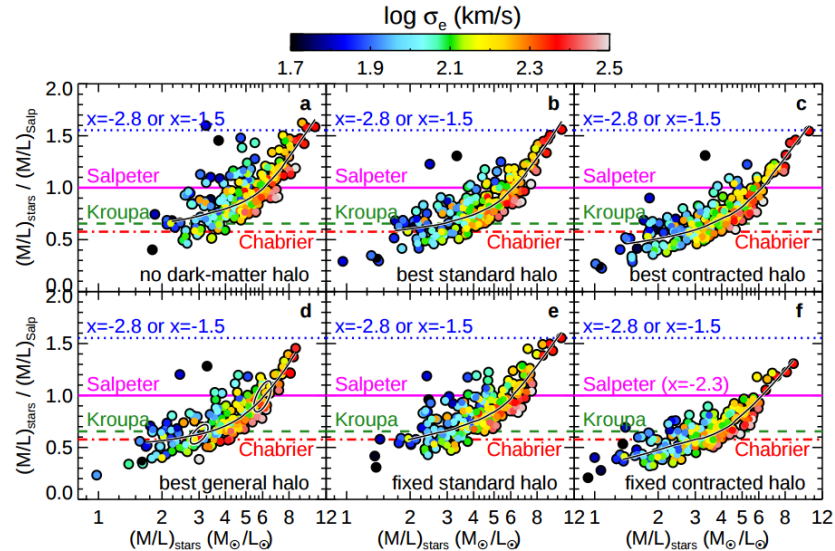


FIGURE 2: The systematic variation of the IMF in early-type galaxies, [Cappellari et al. \(2012\)](#).

Bibliography

- [1] John. Smith, Russell & Lucey. A giant elliptical galaxy with a lightweight initial mass function. *MNRAS*, 000:1–14, 2013.
- [2] Cappellari et. al. Systematic variation of the stellar initial mass function in early-type galaxies. *Nature*, 484:485–488, 2012.
- [3] Gilles Chabrier. Galactic stellar and substellar initial mass function. *The Astronomical Society of the Pacific*, 115:763–795, 2003.
- [4] Pavel Kroupa. On the variation of the initial mass function. *MNRAS*, 322:231–246, 2001.
- [5] Brewer et. al. The swells survey. vi. hierarchical inference of the initial mass functions of bulges and discs. *MNRAS*, 000:1–13, 2012.
- [6] Edwin Salpeter. The luminosity function and stellar evolution. *ApJ*, 121(161), 1955.
- [7] R. F. J. Van der Burg et. al. Evidence for the inside-out growth of the stellar mass distribution in galaxy clusters since $z \approx 1$. *preprint arXiv:1412.2137v2*, 2015.
- [8] Navarro. Frenk & White. The structure of cold dark matter halos. *The Astrophysical Journal*, 462:563–575, 1996.
- [9] Thomas. J et. al. Massive elliptical galaxies: Bh scouring or bottom-heavy imf. *Proceedings IAU Symposium*, (311), 2014.
- [10] Tommaso Treu. Strong lensing by galaxies. *Annual Review of Astronomy ans Astrophysics*, 48:87–125, 2010.
- [11] Smith et al. Stellar dynamics in the strong-lensing central galaxy of abell 1201: A low stellar mass-to-light ratio, a large central compact mass, and a standard dark matter halo. *MNRAS*, (000):1–12, 2017.
- [12] Matthew R. George et. al. Galaxies in x-ray groups. ii. a weak lensing study of halo centering. *The Astrophysical Journal*, 757:2–18, 2012.

- [13] D. Harvey et. al. A detection of wobbling brightest cluster galaxies within massive galaxy clusters. *MNRAS*, 000:1–9, 2017.
- [14] Ramesh. et. al. Narayan. Lectures on gravitational lensing. *Proceedings of the 1995 Jerusalem Winter School. Cambridge University Press*, 1995.
- [15] F. et. al. Courbin. Quasar lensing. *Lecture Notes in Physics, Berlin Springer Verlag*, 608:1, 2002.
- [16] Massimo Meneghetti. Introduction to gravitational lensing. *Lecture Scripts, Heidelberg University*, 2003. URL http://www.ita.uni-heidelberg.de/~massimo/sub/Lectures/gl_all.pdf.
- [17] Teresa. C. O. Wright & Teresa G. Brainerd. Gravitational lensing by nfw halos. *preprint arXiv:astro-ph/9908213v1*, 1999.
- [18] Laigle et. al. The cosmos2015 catalog: Exploring the 1jzj6 universe with half a million galaxies. *The Astrophysical Journal*, 224(2), 2016.
- [19] Cosmos catalogue. 2017. URL cosmos.astro.caltech.edu/.
- [20] Gerard de Vaucouleurs. Sur la technique de l'analyse microphotometrique des nebuleuses brillantes. *Recherches sur les nebuleuses extragalactiques*, 1948.
- [21] Ewa L. Lokas & Gary A. Mamon. Properties of spherical galaxies and clusters with an nfw density profile. *MNRAS*, 321:155–166, 2001.
- [22] C. Sifon et. al. Constraints on the alignment of galaxies in galaxy clusters from $\tilde{1}4000$ spectroscopic members. *A&A*, 575:A48, 2015.
- [23] A. Sonnenfeld et. al. Evidence of dark matter contraction and a salpeter initial mass function in a massive early-type galaxy. *The Astrophysical Journal*, 752:163–180, 2012.
- [24] D. J. Sand et. al. Intracluster supernovae in the multi-epoch nearby cluster survey. *The Astrophysical Journal*, 729:142–155, 2011.
- [25] C. Bildfell et. al. Evolution of the red sequence giant to dwarf ratio in galaxy clusters out to $z \approx 0.5$. *MNRAS*, 425:204–221, 2012.
- [26] Bertin et. al. The terapix pipeline. *Astronomical Data Analysis Software and Systems XI*, 281, 2002. URL <http://adsabs.harvard.edu/abs/2002ASPC..281..228B>.
- [27] Bertin. E & Arnouts. S. SExtractor: Software for source extraction. *Astronomy and Astrophysics*, 117:393–404, 1996.

- [28] Peng et. al. Detailed structural decomposition of galaxy images. *The Astronomical Journal*, 124:266–293, 2002.
- [29] van Dokkum Brammer and Coppi. Eazy: A fast, public photometric redshift code. *ApJ*, 686(1503), 2008.
- [30] Dutton & Maccio. Cold dark matter haloes in the planck era: evolution of structural parameters for einasto and nfw profiles. *MNRAS*, 441:3359–3374, 2014.
- [31] J. C. Munoz Cuartas et. al. The redshift evolution of λcdm halo parameters: concentration, spin and shape. *MNRAS*, 000:1–11, 2010.